FIDVR Capability of Hybrid Grid-Forming PV Power Plants During Feeder Restoration

Abdelrahman M. Mannan, *Graduate Student Member, IEEE*, Hoang P. Dang, *Graduate Student Member, IEEE*, and Hugo N. Villegas Pico, *Senior Member, IEEE*

Abstract—Grid-forming inverters must optimally transfer power from dc-coupled photovoltaic arrays and batteries into an ac grid. Further, they must be able to restore single-phase induction motors (SPIMs) and withstand fault-induced delayed-voltage-recovery (FIDVR) events. These resilience and reliability challenges are addressed here by: (i) engineering a controller to optimally operate dc-coupled hybrid resources; (ii) modeling residential air-conditioning compressors for restoration/FIDVR studies; and (iii) analyzing SPIM thermal-relay performance under limited inverter currents and designing an electronic protection for stalled SPIMs. These contributions are demonstrated via electromagnetic-transient simulations and can be helpful to understand recommendations by the North American Electric Reliability Corporation.

Index Terms—Photovoltaic systems, power generation control, solar power generation.

I. INTRODUCTION

THE U.S. Department of Energy reported that solar technologies could generate as much as 40% of the U.S. electricity supply by year 2035 and 45% by 2050 [1]. Notably, 42% of the 2022 U.S. solar projects were to employ hybrid resources: photovoltaic (PV) arrays and battery energy storage (BES) [2]. Nevertheless, there are several challenges to be solved for the reliable integration of solar assets [1], [3], [4]. For instance, hybrid PV solar resources will be challenged to energize single-phase induction motors (SPIMs) after a blackout and ride through fault-induced delayed voltage recovery (FIDVR) events [1, p. 73].

Historically, restoration of SPIMs has been easily accomplished by synchronous generators [5], [6]. These generators have been also critical to source over-rated currents during FIDVR events to heat up SPIM thermal relays for their disconnection [7, pp. 846–849], [8]. FIDVR events materialize in the form of sustained low voltages that emerge from grid faults that cause the stalling of SPIMs driving residential airconditioning (A/C) compressors [9]. Techniques to alleviate FIDVR include: under-voltage load shedding [10]–[13], varcompensators [14], [15], admittance/impedance detection [16], [17], and motor under-speed tripping [18] to name a few.

At present, grid-forming (GFM) inverter-based resources (IBRs), such as wind and solar, are expected to power the U.S.

This material is based upon work supported by the Power Systems Engineering Research Center under project number S-96, the U.S. Department of Energy, Office of Basic Energy Sciences under award No. DE-SC0021410, and the National Science Foundation under Grant No. 2013739.

A. M. Mannan, H. P. Dang, and H. N. Villegas Pico are with the Department of Electrical and Computer Engineering at Iowa State University, Ames, IA 50011, USA (e-mail: {ammannan, dhphuong, hvillega}@iastate.edu).

grid like synchronous machines have [19]–[22]. However, one problem with this transition is that GFM IBRs powered by hybrid resources are still under research [22], [23]. Further, a major concern is that GFM IBRs cannot source over-rated currents which can jeopardize the starting up of SPIMs and the riding through of FIDVR events [4], [22]. Notably, SPIM restoration and FIDVR problems are likely to persist because residential A/C units are used in 87% of U.S. homes [24].

For the reliable integration of hybrid PV solar resources into the U.S. grid, which also extrapolates worldwide, it is critical to address the following research (R) needs: (R1) A controller for dc-coupled hybrid resources that power GFM IBRs. Present GFM strategies do not consider IBRs powered by dc-coupled PV array and BES, e.g., see [22], [23], [25], [26]. (R2) A realistic compressor model to study restoration and FIDVR events of clusters of SPIMs. Behavioral models [27]-[29] do not capture the compressor nature during SPIM acceleration from stall. Technical documentation by the North American Electric Reliability Corporation (NERC) highlights the need of realistic SPIM modeling [30, p. 16] and their importance for EMT studies [8, p. 1] which are now also recommended for IBRs [31]. Notably, a presentation to the NERC Load Modeling Task Force on August 2017 recommends to revise stall and re-accelerate characteristics of SPIMs [32, p. 4]. (R3) An analysis to understand whether SPIM thermal protection is still viable to mitigate FIDVR events. Present literature has not elucidated the impact of IBR current limiters on thermal protection [22], [23], [33]. (R4) A realistic analysis of the EMT performance of GFM IBRs connected to high-voltage transmission during restoration of distribution feeder, asymmetrical faults, and FIDVR events. In the FIDVR context, classical EMT studies consider that feeders are energized by stiff power sources via high-voltage transmission lines [34], [35]. Further, the dynamic performance of transmission-connected GFM IBRs during restoration and FIDVR events has not been considered in the context of distribution operation, practice, and study requirements, e.g., see [36, pp. 188]. A recent positive-sequence study reports instability of GFM IBRs during FIDVR events [33].

These challenges are addressed here via three contributions:

- A controller for dc-link voltage regulation of GFM IBRs with dc-coupled PV array and BES, q.v. Section III-B. The novelty is the engineering of a strategy to *optimally* charge and discharge the BES under varying solar irradiance which employs anti-windup proportional-integral (PI) regulators.
- 2) A physics-based and computationally-light compressor

1

model with four compression stages, q.v. Section IV-B. The novelty is that it can capture SPIM acceleration, deceleration, and re-acceleration in EMT simulations which contrasts behavioral ones for deceleration only [27]–[29].

3) A demonstration that IBR current limitations will delay the tripping of SPIM thermal relays, implying longer FIDVR events, q.v. Section V-A. Hence, an electronic protection is engineered to disconnect stalled SPIMs by estimating impedance *and* deceleration, q.v. Section V-C. In Section VI-D, it is also shown that this protection satisfactorily operates when electric grids are powered by synchronous machines.

The aforementioned contributions are built on the reliable GFM technology using two-axis anti-windup PI regulators [37]. In this paper, it is not studied instability events when the BES depletes because this is equivalent to study a PV power plant without BES which was already done in [38]. This paper's advances are demonstrated via detailed EMT simulations of dc-coupled hybrid IBRs that are interconnected to high-voltage transmission lines as to power a classical distribution feeder [28]. In the broader impact sense, this paper can be employed to: (i) study the performance of local energyassured generation which NERC identifies as necessary for reliability and resilience [39, p. 3] and (ii) help understand NERC recommendations on EMT simulation of IBRs [31] as well as guidelines on hybrid PV plant performance [40]. Notably, FIDVR events by SPIMs have been a classical concern to NERC [8], [30]–[32], [40]. Here, transmission-connected GFM IBRs can withstand SPIM restoration, transmission faults, and FIDVR events.

The remainder exposition is as follows. Section II discusses the GFM method of [37] as well as restoration and FIDVR events. Section III develops controls for dc-coupled hybrid IBRs. Section IV explains a realistic compressor model. Section V contrasts thermal and electronic relays. Section VI develops four case studies and Section VII concludes.

II. PRELIMINARIES

Figure 1 shows a GFM IBR powered by dc-coupled PV arrays and BES. This technology is considered in this paper because it has higher benefit/cost ratios than PV and storage deployed independently [41, p. v]. Figure 1 exhibits a buckboost converter (BBC), a dc-link capacitor, C_{dc} , a grid-side inverter (GSI), ac inductive-capacitive (LC) filter, and step-up transformer (XFMR). The BBC switches are driven by a buckboost modulator (BBM). The GSI switches are steered by ac voltage/current controllers and an extended sine triangle modulator (ESTM) [42, pp. 483-485]. A set of IBRs connected to a 138-kV transmission line are employed to restore the feeder with SPIMs of Fig. 2. Because a fault is applied to the 138-kV transmission, this paper can be useful to understand: (i) The ability of the hybrid PV grid-forming power plants to ride through faults per FERC order 2023 [43, pp. 1081–1099]. (ii) The capability of these power plants to withstand sustained low voltages events per NERC PRC-024-3 requirements [44].

A. Grid-Forming Strategy

To control the GSI of Fig. 1, this paper adopts the GFM technology of [37], q.v. Fig. 3. The voltage/current controllers use qd-axis anti-windup PI regulators. In Figs. 3a and 3b, $v_{qdf}^c = [v_{qf}^c, v_{df}^c]^{\top}$ and $i_{qdx}^c = [i_{qx}^c, i_{dx}^c]^{\top}$ satisfy [37]:

$$\frac{d}{dt}[v_{qf}^c, v_{df}^c]^{\top} = \frac{1}{\tau_{vf}} \left(-[v_{qf}^c, v_{df}^c]^{\top} + K_v(\theta_c)[v_{abf}, v_{cbf}]^{\top} \right)$$
(1)

$$\frac{d}{dt}[i_{qx}^{c}, i_{dx}^{c}]^{\top} = \frac{1}{\tau_{if}} \left(-[i_{qx}^{c}, i_{dx}^{c}]^{\top} + K_{i}(\theta_{c})[i_{ax}, i_{bx}]^{\top} \right).$$
(2)

Here, $x \in \{f,g\}$ respectively represent currents at: (i) the terminals of the GSI or (ii) the 0.69-kV side of the XFMR in Fig. 1. The quantities $i_{qdf}^{\dagger} = 3C_f\omega_b v_{dqf}^c + i_{qdg}^c$ with $v_{dqf}^c = [v_{df}^c, -v_{qf}^c]^{\top}$ are feedforward currents. The term $3C_f\omega_b v_{dqf}^c$ are speed currents to decouple the impact of q and d components. On the other hand, i_{qdg}^c serves to feedforward asymmetrical transient currents to mitigate their impact on the regulation of ac capacitor voltages. Hence, neither decomposition of qd variables using abstract symmetrical components nor notch filters are necessary to compensate for asymmetrical faulted currents. The time constants τ_{vf} of (1) and τ_{if} of (2) serve to filter current and voltage ripples. The matrices $K_v(\theta_c)$ and $K_i(\theta_c)$ respectively meet [42, p. 112]:

$$K_v(\theta_c) = \frac{2}{3} \begin{bmatrix} \cos(\theta_c) & \cos(\theta_c + 2\pi/3) \\ \sin(\theta_c) & \sin(\theta_c + 2\pi/3) \end{bmatrix}$$
(3)

$$K_i(\theta_c) = \frac{2}{\sqrt{3}} \begin{bmatrix} \cos(\theta_c - \pi/6) & \sin(\theta_c) \\ \sin(\theta_c - \pi/6) & -\cos(\theta_c) \end{bmatrix}.$$
 (4)

The command $v_{qdf}^{\star} = [\sqrt{2/3}v_V V_f^{\star}, 0]$ where V_f^{\star} is a rms line-to-line voltage set-point, v_V is defined in [37, eq. (45)]. In Fig. 3a and 3b, the function $\mathscr{C}: \mathbb{R}^2 \times \mathbb{P} \mapsto \mathcal{U}$:

$$\mathscr{C}\left(u_{qd}^{*}, U_{\text{mx}}\right) = \begin{cases} \frac{U_{\text{mx}}}{U} u_{qd}^{*} & \text{if } U > U_{\text{mx}} \neq 0\\ u_{qd}^{*} & \text{otherwise} \end{cases}$$
 (5)

with $U=\left(u_q^{*2}+u_d^{*2}\right)^{1/2}$ serves to bound u_{qd}^* within an origin-centered circle $\mathcal U$ of radius $U_{\rm mx}$. The principle of $\mathscr C$ in (5) is depicted in Fig. 4 using the qd points u_{qdy}^* , $u_{qdy}^*\in\mathbb R^2$ for $y\in\{a,b\}$ [37]. If $u_{qda}^*\notin\mathcal U$, $u_{qda}^*=\mathscr C(u_{qda}^*,U_{\rm mx})$ is the point at the intersection of the boundary of $\mathcal U$, i.e., $\partial\mathcal U$, and a straight line that joins the center of $\mathcal U$ with u_{qda}^* . If $u_{qdb}^*\in\mathcal U$, then $u_{qdb}^*=u_{qdb}^*$. In the latter case, the controls in Figs. 3a and 3b become the classical PI regulators as shown in [37, Lemma 1].

Remarkably, the function $\mathscr C$ when $U_{\rm mx}=I_{\rm mx}$ maintains GSC current commands i_{qdf}^* in Fig. 3a within the rated current limit $I_{\rm mx}$ during large transients. It also automatically stops integration of z_{qdv} to prevent instability in the unboundedinput unbounded-output sense [37]. In Fig. 3b, $U_{\rm mx}=v_{dc}/\sqrt{3}$ serves to prevent over-modulation of the GSI [38]. The adopted control strategy contrasts those employing two independent univariate anti-windup PI regulators [46] which signify that qd commands are bounded in a square $\mathcal Q$ in lieu of a circle $\mathcal U$, q.v. Fig. 4. Please, note that $\mathcal Q$ over-approximates $\mathcal U$. For example, the command u_{qda}^* in Fig. 4 would not be

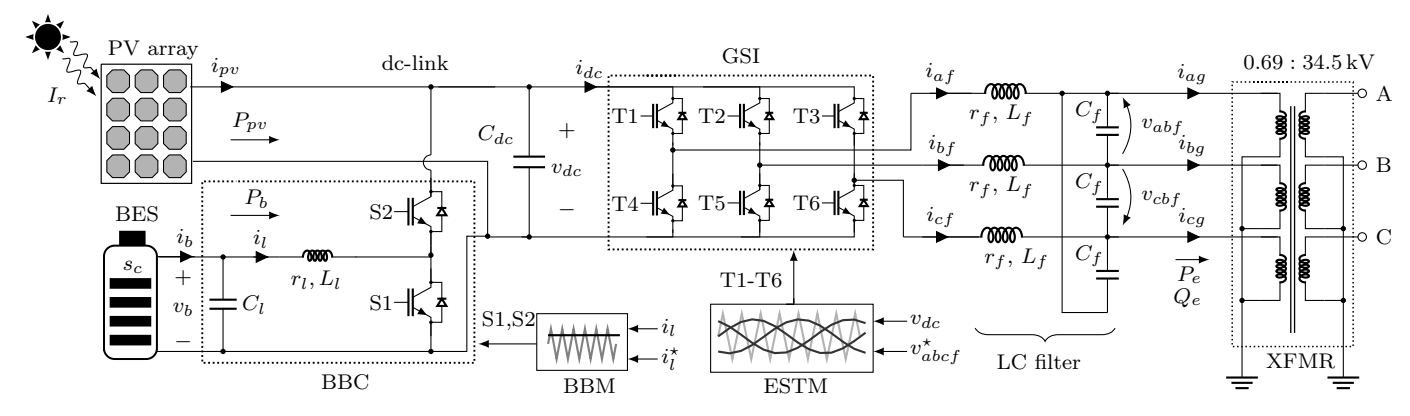


Fig. 1. Grid-forming subsystem including PV array, battery energy storage (BES), buck-boost converter (BBC), buck-boost modulator (BBM), grid-side inverter (GSI), extended sine-triangle modulator (ESTM), and step-up transformer (XFMR) [40].

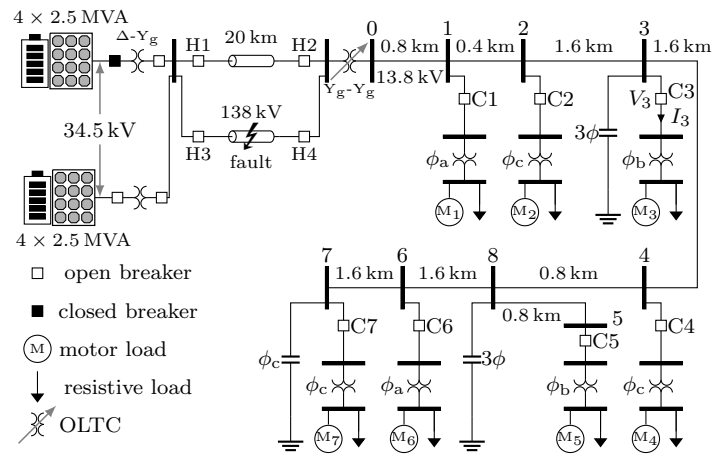


Fig. 2. Radial feeder with clusters of single-phase motor and resistive loads [28]. Each cluster has 177×5.3 -kW motors and 177×1.1 -kW resistive loads. Here, for example, ϕ_a and 3ϕ signify a-phase and 3-phase connections.

bounded in \mathcal{U} if using independent anti-windup PI regulators as belonging to \mathcal{Q} .

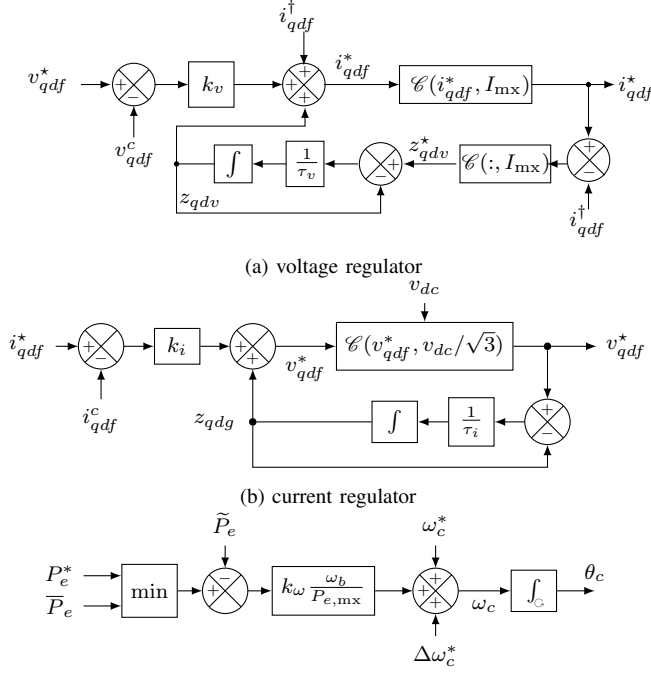
The reference frame angle $\theta_c \in [0, 2\pi)$ for (3) and (4) is from Fig. 3c. There, k_ω is a droop constant, ω_b is the base angular frequency, $P_{e,\text{mx}}$ is rated electric power, and $\widetilde{P_e}$ is filtered electric power satisfying:

$$\frac{d}{dt}\widetilde{P_e} = \frac{1}{\tau_e} \left(-\widetilde{P_e} + P_e \right) \tag{6}$$

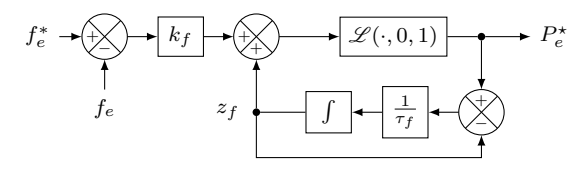
with $P_e=3/2\left(v_{qf}^ci_{qg}^c+v_{df}^ci_{dg}^c\right)$ from (1) and (2). The filter in (6) serves to attenuate double frequency components in power fluctuations caused by unbalanced operation and asymmetrical faults. The set points ω_c^* and P_e^* in Fig. 3c are used for dc-link voltage protection and frequency control, respectively.

During a fault, $P_e \to 0$ in Fig. 3c, thus $P_e \to 0$ (6) leading to an increased of ω_c in Fig. 3c. If $P_e \to 0$, the dc-link voltage v_{dc} will also increase. However, it will be quickly driven to its set-point via the dc-link controllers of Section III-B [see also Fig. 22-E]. Meanwhile, the regulators of Figs. 3a and 3b will attempt to control the ac capacitor voltages by regulating the GSI terminal currents (q.v., Fig. 1) until the limit $I_{\rm mx}$ is reached. The combination of these control loops makes a holistic fault ride-through strategy.

In assets using synchronous machines, similarly, the electric power transferred from the primer mover into the grid via the synchronous machine drops close to zero during faults.



(c) modified droop-control law [37], [38], [45]



(d) power-plant frequency controller [37]

Fig. 3. Grid-forming voltage and current PI regulators as well as droop-control law. The integrator of the droop law wraps $\theta_c \in [0, 2\pi)$ rad.

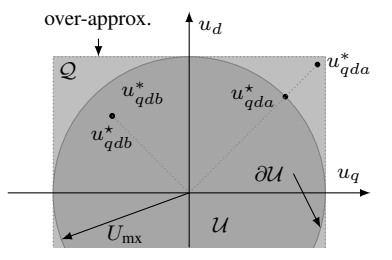


Fig. 4. Principle of $\mathscr C$ in (5) and Fig. 3, taken from [37].

Then, the machine rotor accelerates which is sensed by its governor which tries to regulate speed by controlling the flow of gas, water, or steam into the prime mover. Meanwhile, the machine voltage regulator increases the excitation level in an attempt to rise terminal voltages until reaching the voltage regulator limits. Of course, this happens at a much slower time scale than what occurs in the system of Fig. 1. Although it is possible to make the controls of the GSI and the BBC slow acting as in conventional generators, the dc-link voltage, for example, can collapse [38] because dc-link energy storage capacity is not as large as in the rotor of a generator.

If the BES of Fig. 1 depletes, the variable $\Delta\omega_c^*$ in Fig. 3c protects the dc-link voltage from collapsing by reducing speed, ω_c [38]. This in turn decreases the amount of power the GSI transfers to the grid, P_e , so that it is less than the maximum power the PV array can produce, i.e.,

$$P_{pv}^* = \max_{v_{dc}} P_{pv}(v_{dc}) \tag{7}$$

which is estimated by following [38]. The flow of P_e and P_{pv} are shown in Fig. 1. The operator $\min\{P_e^*, \overline{P}_e\}$ in Fig. 3c ensures P_e^* is not greater than \overline{P}_e . If the BES has depleted $\overline{P}_e = P_{pv}^*$; otherwise, $\overline{P}_e = P_{e,\text{mx}}$ which is rated electric power. Here, the command P_e^* satisfies:

$$\frac{d}{dt}P_e^* = \frac{1}{\tau_n} \left(-P_e^* + P_{e,\text{mx}} P_e^* \right) \tag{8}$$

with P_e^* the output of the secondary frequency control loop in Fig. 3d which is a power-plant controller that has already been developed in [37]. Note here that a common per-unit P_e^* is broadcasted to all IBRs within a power plant. Each IBR, nonetheless, limits this command via $\min\{P_e^*, \overline{P}_e\}$ in Fig. 3c.

The ESTM commands $v_{abcf}^{\star} = [v_{af}^{\star}, v_{bf}^{\star}, v_{cf}^{\star}]^{\top}$ in Fig. 1 are mapped from v_{qdf}^{\star} in Fig. 3b [42] via:

$$\begin{bmatrix} v_{af}^{\star}, v_{bf}^{\star}, v_{cf}^{\star} \end{bmatrix}^{\top} = T^{\top}(\theta_c) \begin{bmatrix} v_{qf}^{\star}, v_{df}^{\star} \end{bmatrix}^{\top}$$
(9)
$$T(\theta_c) = \begin{bmatrix} \cos(\theta_c) & \cos(\theta_c - 2\pi/3) & \cos(\theta_c + 2\pi/3) \\ \sin(\theta_c) & \sin(\theta_c - 2\pi/3) & \sin(\theta_c + 2\pi/3) \end{bmatrix}.$$
(10)

B. Restoration of Distribution Feeders

GFM IBRs are challenged here to start up clusters of SPIM loads and withstand FIDVR during restoration because of GSI current limitation [33], [47]. At present, FERC and NERC have reported that restoration plans of legacy systems consider instances of locked-rotor currents by three-phase motors [5, p. 34]. In the future, this consideration might be extended to the energization of SPIMs because they also cause locked-rotor inrush currents. Notably, the dynamic response of SPIMS has been a classical concern to NERC [8], [30]-[32], [40]. In Fig. 2, eight 2.5-MVA GFM IBRs as the one in Fig. 1 are challenged to energize 6.6-MW c.a. of SPIMs driving (compressors and condenser fans) and 1.4-MW of resistive loads. There, $4 \times 2.5 \,\mathrm{MVA}$ signifies that only one 2.5-MVA grid-forming subsystem, as the one in Fig. 1, is simulated. Nonetheless, its three-phase current outputs are amplified by 4 times at the 34.5-kV side using a standard scaling technique [48]. This approach is adopted in Section VI to reduce computational burden because of semiconductor switching simulation, see Fig. 1.

A possible restoration plan for the grid in Fig. 2 is: (i) energize the 10-MVA 34.5/138-kV Δ -Yg transformers of each PV plant by closing their circuit breakers; (ii) energize the 138-kV overhead transmission lines by closing H1–H4 which in turn power the Yg-Yg transformer and buses '0' to '8'; and (iii) sequentially energize each cluster of 177 SPIMs driving A/C compressors and resistive loads by closing breakers C1 to C7. The on-load tap changer (OLTC) [next to bus '0' in Fig. 2] serves to compensate for voltage drops in the 138-kV transmission lines as well as the Δ -Yg and Yg-Yg transformers. Next, this paper develops the technology to materialize the restoration of feeders using hybrid IBRs.

III. CONTROL OF HYBRID RESOURCES

The main novelty of this section is a control strategy for the BBC and the BBM as to charge or discharge the BES, q.v. Fig. 7. From Fig. 1, one can realize that the battery may be charged if: (i) the power transferred to the ac grid P_e (plus losses) is less than the maximum PV power P_{pv} and (ii) the state of charge (SoC), s_c is less than the maximum SoC, \overline{s}_c . Conversely, the battery may be discharged if: (i) P_e (plus losses) is greater than the maximum P_{pv} and (ii) s_c is greater than the minimum SoC, \underline{s}_c . This task is achieved by calculating an optimal dc voltage set-point as explained next.

A. Dc Voltage Set-Point for Optimal Hybrid Operation

The sense of optimality here is to estimate the voltage set-point v_{dc}^* so that $P_{pv}(v_{dc}^*)$ of Fig. 1 is maximum. Recall from (7) that $P_{pv}^* = P_{pv}(v_{dc}^*)$; v_{dc}^* and P_{pv}^* are illustrated in Fig. 5a. For grid-forming operation, $v_{dc} \in [v_{dc}^*, v_{dc}^o]$ to extract any $P_{pv} \in [0, P_{pv}^*]$; v_{dc}^o is the open circuit voltage of the PV array. When $s_c < \overline{s}_c$ and $P_{pv}^* > P_e$ of (6), v_{dc}^* serves in Section III-B to charge the BES with the remainder power which approximates to $P_{pv}^* - P_e$ because of losses. When $s_c \geq \overline{s}_c$ and $P_{pv}^* > P_e$, the BES is not charged, hence v_{dc} increases until P_{pv} matches P_e plus losses, see Fig. 1 and 5a. If $s_c < \overline{s}_c$ and $P_e > P_{pv}^*$, $v_{dc} \to 0$, i.e., dc-link voltage will collapse if there is no dc-link protection [38].

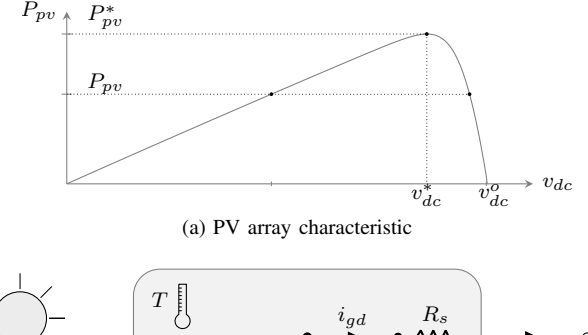
In this paper, the voltage set-point v_{dc}^{*} is estimated as done in [38] by using an abstract model of the PV array as well as measured voltage v_{dc} and current i_{pv} , see Fig. 1. The PV array in Fig. 1 comprises of N_p parallel-connected strings, each of which has N_s series-connected PV modules. Each module is modeled using a single-diode equivalent circuit, q.v. Fig. 5b. There, the light-generated current $i_g = (i_{g,\text{nom}}/I_{r,\text{nom}})\,I_r$ for a given solar irrandiance level $I_r > 0$. The parameters $i_{g,\text{nom}}$ and $I_{r,\text{nom}} = 1000 \text{ W/m}^2$ are nominal light-generated current and solar irradiance, respectively. From measured v_{dc} and v_{gc} in Fig. 1, an estimation of the light-generated current, v_{gc} of each PV module in Fig. 5b is [38]:

$$\hat{i}_g = i_d + i_{sh} + i_{pv}/N_p \text{ where } i_d = i_0 \left(e^{\frac{v_d}{v_T}} - 1\right)$$
 (11)

$$v_d = v_{dc}/N_s + R_s i_{pv} \text{ and } i_{sh} = v_d/R_{sh}$$
 (12)

¹The behavior of P_{pv} vs. v_{dc} is illustrated in Fig. 5a.

 $^{^2\}mathrm{Here},~i_g$ is considered proportional to solar irradiance $I_r,$ which is assumed uniform across the PV array [38].



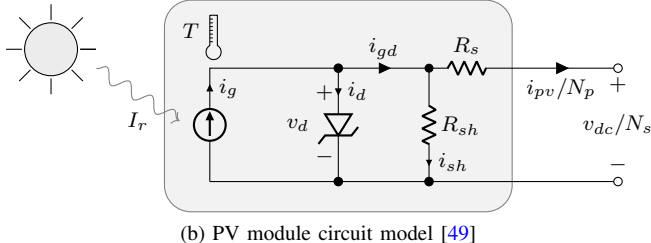


Fig. 5. PV array characteristic and PV module circuit model.

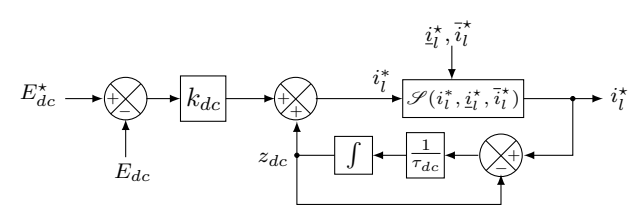


Fig. 6. Dc-link voltage PI regulator to control v_{dc} of Fig. 1.

which serves as input to calculate the $v_d = v_d^*$ that maximizes:

$$\frac{P_{pv}(v_d)}{N_s N_p} = v_d i_{gd}(v_d) - R_s \left(i_{gd}(v_d) - \frac{v_d}{R_{sh}} \right)^2 - \frac{v_d^2}{R_{sh}}$$
(13)
$$\text{where } i_{gd}(v_d) = \hat{i}_g - i_0 \left(e^{\frac{v_d}{v_T}} - 1 \right) .$$
(14)

For (11)–(14): (i) the parameters R_s and R_{sh} as well as the variables i_g (and estimated \hat{i}_g), v_d , and i_d are illustrated in Fig. 5b and (ii) the parameters v_T and i_0 are defined in [49].

The maximizer $v_d = v_d^*$ is unique because $P_{pv}(v_d)$ of (13) is concave on v_d [38]. Hence, v_d^* is uniquely determined by computing the zero of $dP_{pv}(v_d)/dv_d$ via convergent Newton-Raphson iterations [38]. The optimal v_{dc}^* is obtained from:

$$v_d^* = \frac{R_{sh}}{R_s + R_{sh}} \left(\frac{v_{dc}^*}{N_s} + R_s i_{gd}(v_d^*) \right). \tag{15}$$

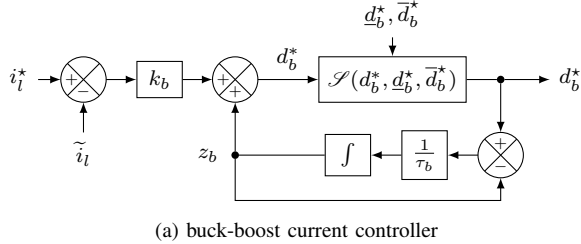
Note that $i_{qd}(v_d)$ is defined in (14) and shown in Fig. 5b.

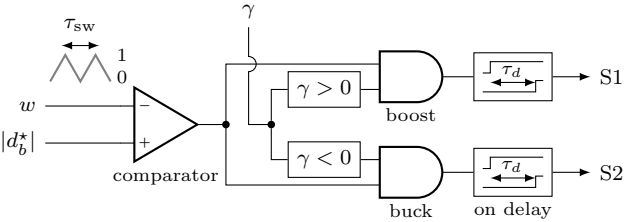
B. Dc-Link Voltage Control

The novelty of this subsection is a control strategy to regulate the dc-link voltage, v_{dc} , of the GFM in Fig. 1. The strength of the proposed dc-link voltage control strategy is its simplicity which is important for industry adoption. In particular, v_{dc} is regulated by steering the dc-link capacitor energy $E_{dc} = \frac{1}{2} C_{dc} v_{dc}^2$ so that it follows the set-point:

$$E_{dc}^* = \frac{1}{2} C_{dc} \max\{(v_{dc}^*)^2, (v_{mn})^2\}$$
 (16)

where v_{dc}^* is from (15) for maximum PV power harvesting. Here, v_{mn} ensures maintaining minimum dc-link voltage during low irradiance events for GSI control [38].





(b) buck-boost modulator (BBM)

Fig. 7. Buck-boost current controller and its modulator to control i_l of Fig. 1.

Specifically, the regulation of E_{dc} (or v_{dc}) is achieved by steering i_l of Fig. 1 so that it follows:

$$i_l^* = \mathcal{S}(i_l^*, \underline{i}_l^*, \overline{i}_l^*) \text{ with } i_l^* = k_{dc}(E_{dc}^* - E_{dc}) + z_{dc}$$
 (17)
and $\frac{d}{dt}z_{dc} = \frac{1}{\tau_{dc}}(-z_{dc} + i_l^*)$. (18)

This control law, shown in Fig. 6, is a one-axis or univariate PI regulator with anti-windup capability [37]. The parameters k_{dc} and τ_{dc} are the proportional and integration-time constants, respectively. The saturation function: $\mathscr{S}: \mathbb{R} \times \mathbb{P} \times \mathbb{P} \to \mathbb{R}$:

$$\mathcal{S}(\chi, \underline{\chi}, \overline{\chi}) = \begin{cases} \chi & \text{if } \chi \in [\underline{\chi}, \overline{\chi}] \\ \underline{\chi} & \text{if } \chi < \underline{\chi} \\ \overline{\chi} & \text{if } \chi > \overline{\chi}. \end{cases}$$
(19)

of (17) serves to: (i) ensure the BES SoC $s_c \in [\underline{s}_c, \overline{s}_c]$ and (ii) ensure the command $i_l^\star \in [\underline{i}_l, \overline{i}_l]$. Specifically, for (17):

$$\overline{i}_{l}^{\star} = \begin{cases} 0 & \text{if } s_{c} \leq \underline{s}_{c} \\ \overline{i}_{l} & \text{if } s_{c} > \underline{s}_{c} \end{cases} \text{ and } \underline{i}_{l}^{\star} = \begin{cases} \underline{i}_{l} & \text{if } s_{c} < \overline{s}_{c} \\ 0 & \text{if } s_{c} \geq \overline{s}_{c} \end{cases}$$
 (20)

In this paper, it is assumed that s_c is observable; \underline{s}_c and \overline{s}_c are minimum and maximum SoC limits. Next, i_l^{\star} of (17) steers the BBC of Fig. 1 for charging or discharging the BES.

In some instances, $s_c \leq \underline{s}_c$ and $P_e > P_{pv}^*$ [P_e and P_{pv}^* are from Section II-A]; hence, $v_{dc} \to 0$; i.e., v_{dc} may collapse. As indicated in Section II-A, voltage collapse can be prevented by steering $\Delta \omega_c^*$ of Fig. 3c. Nonetheless, this approach can also cause the decline of the ac frequency, f_e , while maintaining an acceptable volts-per-hertz ratio as to make the frequency-and voltage-sensitive loads withdraw less power from the IBRs [37]. Please, note that \overline{P}_e of Fig. 3c limits the action of frequency control according to P_{pv}^* if frequency declines. Because this idea has been already developed for grid-forming PV power plants without BES [38], this approach is not discussed in this paper.

C. Buck-Boost Control

The novelty of this subsection is the current controller and the BBM of Fig. 7 which uses one-axis anti-windup PI regulators. They are engineered to steer the BBC of Fig. 1 for charging and discharging the BES as well as the seamless

grid-forming operation of the GSI. In particular, the mission of the current controller in Fig. 7a is to drive $i_l \rightarrow i_l^*$ of (17) by generating modulation index command, d_h^* .

The modulator in Fig. 7b generates PWM commands to turn on and off the switches S1 and S2 in Fig. 1 to discharge and charge the BES, respectively. The buck or boost mode in Fig. 7b is selected via:

$$\gamma = \begin{cases} 1 & \text{if } d_b^{\star} > \epsilon_b \text{ for boost mode} \\ -1 & \text{if } d_b^{\star} < -\epsilon_b \text{ for buck mode} \\ 0 & \text{otherwise.} \end{cases}$$
 (21)

Here, ϵ_b is a small deadband to prevent switching S1 and S2 when $|d_b^{\star}| \leq \epsilon_b = 0.001$, for example.

In this paper, the modulation index set-point satisfies:

$$d_b^{\star} = \mathscr{S}(d_b^{\star}, \underline{d}_b^{\star}, \overline{d}_b^{\star}) \text{ with } d_b^{\star} = k_b(\widetilde{i}_l - i_l^{\star}) + z_b$$
 (22)

and
$$\frac{d}{dt}z_b = \frac{1}{\tau_b} \left(-z_b + d_b^{\star} \right) \tag{23}$$

which is the anti-windup PI regulator on the top of Fig. 7a. The parameters k_b and τ_b are proportional and integration-time constants. The filtered current \widetilde{i}_l in (22) satisfies:

$$\frac{d}{dt}\widetilde{i}_{l} = \frac{1}{\tau_{l}} \left(-\widetilde{i}_{l} + i_{l} + \Delta i_{l} \right) \tag{24}$$

with i_l in Fig. 1 and Δi_l an unknown-but-bounded sensing error. The limits \overline{d}_b^\star and \underline{d}_b^\star of (22) satisfy:

$$\overline{d}_b^* = \begin{cases} 1 & \text{if } s_c > \underline{s}_c \\ 0 & \text{otherwise} \end{cases} \text{ and } \underline{d}_b^* = \begin{cases} -1 & \text{if } s_c < \overline{s}_c \\ 0 & \text{otherwise.} \end{cases}$$
 (25)

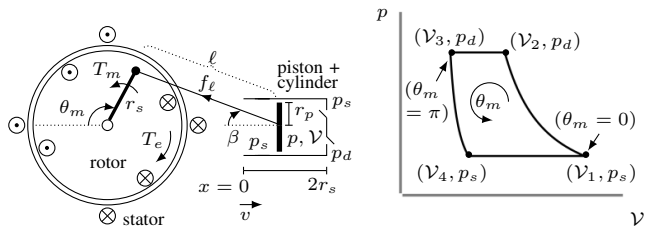
They serve to not overcharge the BES if the SoC, s_c , is too high and block battery discharging if s_c is too low. Because of (25), the proposed implementation will not result in unintended trickle charging or depletion of the battery if the SOC reaches its limits and $|\Delta i_l| > 0$ in (24).

Please note in Fig. 7a that the modulation index d_b^{\star} of (22) is a command to the BBM in Fig. 7b. Also, note in Fig. 7b that $|d_b^{\star}|$ is compared against a triangular waveform w with switching period $\tau_{\rm sw}$ for activation of S1 and S2. The switch activation commands, S1 and S2, are delayed by τ_d to prevent shoot-through instances [42, p. 420].

D. Standard Optimization Problem

The controls in Sections III-A-III-C are summarized here as a standard optimization problem to solidify understanding:

$$\begin{aligned} & \underset{v_{dc},i_{l}}{\text{max.}} & P_{pv} \\ & \text{s. t.} & & \frac{P_{pv}}{N_{s}N_{p}} = v_{d}i_{gd} - R_{s}\left(i_{gd} - \frac{v_{d}}{R_{sh}}\right)^{2} - \frac{v_{d}^{2}}{R_{sh}} \\ & & i_{gd} = \hat{i}_{g} - i_{0}\left(e^{\frac{v_{d}}{v_{T}}} - 1\right) \\ & & v_{d} = \frac{R_{sh}}{R_{s} + R_{sh}}\left(\frac{v_{dc}}{N_{s}} + R_{s}i_{gd}\right) \\ & & v_{dc} \geq v_{\text{mn}} \\ & & P_{e} - P_{pv} - P_{b} = 0 \\ & & P_{b} = i_{l}v_{b} \\ & & & \underline{i}_{l}^{\star}(s_{c}) \leq i_{l} \leq \overline{i}_{l}^{\star}(s_{c}) \,. \end{aligned}$$



(a) motor and compressor assembly

(b) p vs. \mathcal{V} behavior

Fig. 8. Motor-compressor assembly and compressor pressure vs. volume characteristic. Only one piston-cylinder set out of two is illustrated.

Here, the overall objective is to maximize photovoltaic power P_{pv} from (13)–(15) as to: (i) charge the BES by regulating power, P_b , and (ii) inject electric power, P_e , to meet the demand, q.v. Fig. 1. This is achieved by steering dc-link voltage $v_{dc} \rightarrow v_{dc}^*$ of (16) and current $i_l \rightarrow i_l^*$ of (17); the decision variables v_{dc} and i_l are illustrated in Fig. 1. In (26), P_e of (6), \hat{i}_g of (14), and s_c of (20) are exogenous inputs to the optimization problem. The BES voltage v_b is treated as constant there. Because the problem (26) can become physically infeasible, additional strategies to also control P_e can be employed, see [37], [38]. The inequality constraints $v_{dc} \geq v_{\rm mn}$ and $\underline{i}_l^*(s_c) \leq i_l \leq \overline{i}_l^*(s_c)$ [depending on s_c] are from (16) and (20), respectively.

For formulation simplicity of (26), losses as well as the dynamics of v_{dc} , i_l , and v_b in Fig. 1 are not considered. It is necessary to clarify, nonetheless, that the problem in (26) is tackled in Sections III-A–III-C via a set of cleverly engineered anti-windup PI regulators which are applied to a realistic EMT model in Section VI.

IV. COMPRESSOR MODEL

The novelty is a physics-based or realistic model of a residential A/C compressor, q.v. Fig. 8. This model is critical for EMT studies of restoration and FIDVR events involving GFM IBRs. Compressor modeling is labeled as complicated [28]; thus, behavioral models are used [27]–[29]. In Section VI-B, the CPU times when simulating power systems using the realistic and behavioral compressor models are comparable; they employ 44 and 43 minutes of CPU time, respectively.

A. Behavioral Compressor Model

A motor-compressor subsystem is depicted in Fig. 8. A SPIM is used to drive two piston-cylinder assemblies [50]. In Fig. 8a, the rotor angular speed, ω_m , and position, θ_m meet:

$$\frac{d}{dt}\omega_m = \frac{1}{J}(T_e - T_m) \text{ and } \frac{d}{dt}\theta_m = \omega_m.$$
(27)

The inertia constant, J, aggregates the impact of the rotor, pistons, and counterweights [50] on rotor dynamics; assume rigid connecting rods of length ℓ .³ The nature of electrical torque, T_e , has been rigorously modeled [28], [52], [53]; but, the mechanical torque, T_m , has been behaviorally represented [8], [28], [54]. Because T_e and T_m in (27) are algebraically additive, they are both important to be modeled for restoration and FIDVR analyses.

³Considering flexible rods is complex and computationally expensive [51].

Behaviorally, $T_m \approx T_{\rm speed} + T_{\rm av}$ for (27) where [28]: (i) $T_{\rm speed}$ is proportional to ω_m^2 and (ii) $T_{\rm av}$ (of triangular shape) is dependent on θ_m and a user-defined amplitude. Specifically,

$$T_m \approx \underbrace{k_\omega \omega_m^2}_{T_{\text{speed}}} + \underbrace{2k_{\text{av}}\left(1 - \left|\frac{2\theta_m}{\pi} - 1\right|\right)}_{T_{\text{min}}}$$
 (28)

where k_{ω} and $k_{\rm av}$ are user defined parameters to model the T_{speed} and T_{av} components, respectively. The angle θ_m for (28) is assumed to be wrapped within $[0, 2\pi)$. In present EMT implementations of (28), k_{av} is kept at zero until the SPIM rotor has surpassed a certain speed in time [27, p. 26–27]. This signifies that the compressor is modeled as a fan because only the T_{speed} component is active. More importantly, it is never discussed when k_{av} should be deactivated if the SPIM decelerates and/or reactivated if it re-accelerates during and after a FIDVR event. Such simulation practice constraints engineers to simulate SPIM impacts on restoration and FIDVR events if the rotor does not accelerate due to high compressor torque, low ac voltage, or wrong choice of start-run capacitors. In some cases, even if SPIMs stall, they may re-accelerate after a fault is cleared. Hence, compressor models that capture acceleration, deceleration, and re-acceleration must be considered in an EMT study to capture both restoration and FIDVR events which cannot be done with a behavioral model. A realistic compressor model follows.

B. Realistic Compressor Model

The parameters and variables to model a reciprocating compressor are shown in Fig. 8a. The physical model of a reciprocating compressor is comparable to the dynamics of a slidercrank mechanism [55], [56]. High-fidelity compressor models consider flexible rods which are computationally expensive to simulate [51], [55]. Indeed, the dynamics of discharge and intake valves as well as compressor thermal processes are also complex to simulate [57], [58]. This subsection develops a model that realistically captures the mechanical behavior of a reciprocating compressor and is as computationally-light as the behavioral one in Section IV-A. In the proposed model, flexible rods and compressor thermal processes are omitted because elasticity phenomena of materials and thermal efficiency might not be critical factors in restoration and FIDVR events. The novelty is that the complexities of the dynamics of the discharge and intake valves are modeled as function of rotor position to alleviate computational burden.

Realistically, the torque T_m for (27) meets:

$$T_m = D_p \omega_m^2 + T(\theta_m, \omega_m) + T(\theta_m + \pi, \omega_m)$$
 (29)

if $|\omega_m|>0$; otherwise, $T_m=0$. In (29): (i) $D_p\omega_m^2$ is from an oil pump and (ii) $T(\theta_m,\omega_m)$ and $T(\theta_m+\pi,\omega_m)$ are by

two twin compressor pistons that are π rad out of phase [50]. Specifically:

$$T(\theta_m, \omega_m) = \left(\sin \theta_m \cos \beta - \frac{r_s}{2\ell} \sin 2\theta_m\right) r_s f_\ell \qquad (30)$$

where
$$f_{\ell}\cos\beta = D_f v + f_p$$
 (31)

and
$$\cos \beta = \sqrt{1 - \frac{r_s^2}{\ell^2} \sin^2 \theta_m}$$
 (32)

under the assumption of stiff connecting rods of length ℓ , each transmitting force f_{ℓ} , q.v. Fig. 8a. Note that (30) is from the component of f_{ℓ} that is perpendicular to the radius r_s . Also, the horizontal projection of f_{ℓ} in (31) transmit the forces developed by piston friction $D_f v$ and cylinder pressure f_p . In (31), D_f is a friction constant and v is the piston speed:

$$v(\theta_m, \omega_m) = r_s \omega_m \sin \theta_m - \frac{1}{2} \frac{\omega_m \ell}{\cos \beta} \frac{r_s^2}{\ell^2} \sin 2\theta_m.$$
 (33)

Further, the force, f_p , developed by the gas-refrigerant pressure pressure p in a sealed compressor for (31) satisfies:

$$f_p = \pi r_p^2 (p - p_s)$$
. (34)

In Fig. 8b, the behavior of p vs. V for *isentropic*⁵ compression, discharge, expansion, and intake stages satisfies:

$$p = \begin{cases} \min \left\{ p_s \left(\frac{\mathcal{V}}{\mathcal{V}_1} \right)^{m_{12}}, p_d \right\} & \text{if } |\theta_m| \in [0, \pi) \\ \max \left\{ p_s \left(\frac{\mathcal{V}}{\mathcal{V}_4} \right)^{m_{34}}, p_s \right\} & \text{otherwise} \end{cases}$$
(35)

with
$$V = V_3 - \frac{V_1 - V_3}{2r_s} (x - 2r_s)$$
, (36)

$$m_{12} = \frac{\ln \frac{p_d}{p_s}}{\ln \frac{\mathcal{V}_2}{\mathcal{V}_s}}, \text{ and } m_{34} = \frac{\ln \frac{p_d}{p_s}}{\ln \frac{\mathcal{V}_3}{\mathcal{V}_s}}.$$
 (37)

In (34) and (35), p_s is the suction pressure and p_d the discharge pressure. The min and max operators in (35) serve to automatically switch the discharge-to-expansion and intake-to-compression processes at $|\theta_m| = \pi$ and $|\theta_m| = 2\pi$, respectively, q.v. Fig. 8b. This novelty relieves the complex task of modeling the dynamics of discharge and intake valves, e.g., see [50]. In (36), the piston position $x \in [0, 2r_s]$ is from:

$$x(\theta_m) = r_s - r_s \cos \theta_m + \ell \cos \beta - \ell. \tag{38}$$

Please, note that p of (35) and \mathcal{V} of (36) depend on θ_m of (27). Also, (30) requires computationally light operations via (31)–(38) for given θ_m and ω_m from (27).

It is important to point out that the realistic compressor model from (29) to (37) requires eleven parameters: r_s , r_p , l, p_s , p_d , \mathcal{V}_1 , \mathcal{V}_2 , \mathcal{V}_3 , \mathcal{V}_4 , D_f , and D_p , q.v. Fig. 8. This contrasts the two parameters k_ω and $k_{\rm av}$ in the behavioral model of (28). The parameters of the realistic compressor model can be obtained from a datasheet or manuals [59], [60] or by physically disassembling a compressor [50].

Further, it is instructional to show that the proposed model driven by a SPIM resembles reported experimental data. In particular, Fig. 9 contrasts the active, P, and reactive, Q, power withdrawn by a SPIM driving the proposed realistic model versus voltage magnitude V. In a simulation that

⁴A presentation to the NERC Load Modeling Task Force recommended to revise stall and re-accelerate characteristics of SPIMs [32].

⁵Compressor thermodynamic processes [58] are disregarded

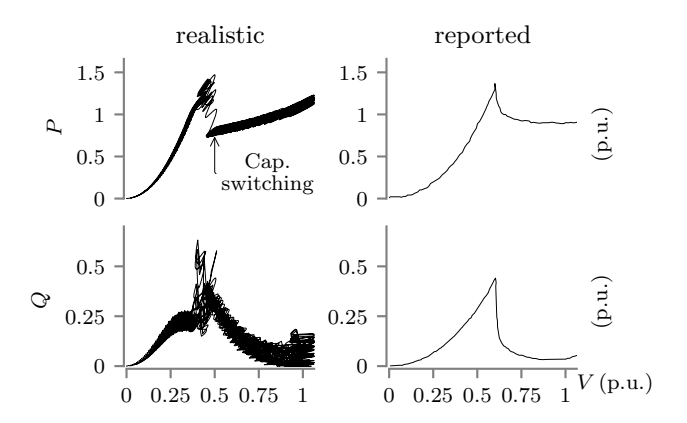


Fig. 9. SPIM active and reactive power vs. terminal voltage. The simulation of the realistic model is compared against reported data [8, p. 19].

mimics [8, p. 19], V is decreased from 100% to 0.0% in 2 seconds [the model parameters are in Table III]. The results are contrasted against observations reported in [8, p. 19] for a temperature of $80\,\mathrm{F}$. Overall, the simulation results considering the realistic compressor resemble the reported data in [8, p. 19]. The discrepancy between the realistic and reported reactive power is because this quantity is sensitive to the parameters of the SPIM model and start-run capacitors which are not reported in [8, p. 19]; hence, generic parameters were employed, q.v. Table III. Notice the realistic simulation results were not filtered; the oscillations of P and Q are natural in single phase systems.

V. MOTOR STALLING PROTECTION

It is shown here that thermal relays will face longer tripping times to disconnect stalled SPIMs when powered by IBRs than by synchronous machines. Further, if IBR current is not sufficient, thermal relays might not trip at all. Thus, an electronic protection is engineered which consists of estimating SPIM impedance and acceleration.

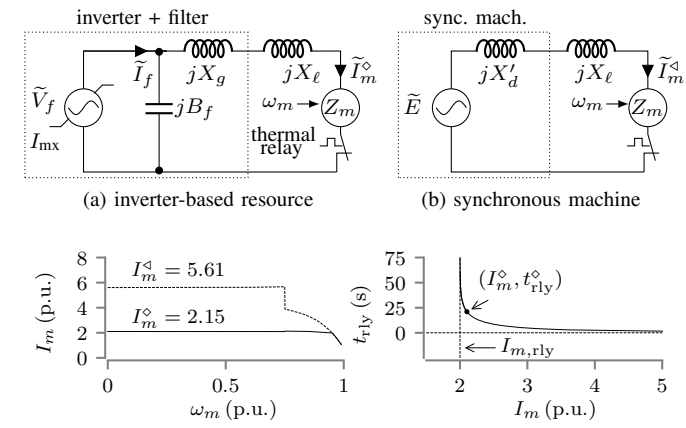
A. Classical Thermal Protection

The tripping time of a thermal relay is [61]:

$$t_{\rm rly} = \tau_{\rm rly} \ln \left(\frac{I_m^2 - I_{m,\rm opr}^2}{I_m^2 - I_{m,\rm rly}^2} \right) \text{ for } I_m > I_{m,\rm rly} \,.$$
 (39)

Here, $\tau_{\rm rly}$ is the relay thermal time constant, I_m is the present rms current of the SPIM undergoing stalling, $I_{m,{\rm opr}}$ is the rms current of a SPIM previous to stalling, and $I_{m,{\rm rly}}$ is the pick-up current of the thermal relay. In this paper, $I_m \in \{I_m^{\diamond}, I_m^{\lhd}\}$ where I_m^{\diamond} and I_m^{\lhd} are respectively the SPIM rms currents produced by an IBR and a machine, q.v. Fig. 10a and 10b. Note here that if I_m^{\diamond} is not greater than $I_{m,{\rm rly}}$, the thermal relay will not pickup.

In Fig. 10c, I_m^{\diamond} and I_m^{\diamond} can be as high as 2.15 p.u. and 5.61 p.u., respectively. Hence, the thermal relay can trip only as fast as $t_{\rm rly}^{\diamond}=13.24\,{\rm s}$ and $t_{\rm rly}^{\diamond}=1.44\,{\rm s}$ if $\omega_m=0$ (i.e., when the motor stalls) for the inverter and machine cases, respectively. Notably, a tripping time of $t_{\rm rly}^{\diamond}=13.24\,{\rm s}$ is relatively long with respect to $t_{\rm rly}^{\diamond}=1.44\,{\rm s}$. Hence, an approach to stalling protection for converter-based grids is proposed in Section V-C and



(c) motor current and thermal-relay tripping time

Fig. 10. Current-limited inverter and a synchronous machine powering a single-phase motor as well as its thermal relay tripping time.

tested in the EMT domain in Section VI. In Fig. 10, the ratings of the IBR and the synchronous machine are assumed to be twice of that of the SPIM. To generate Fig. 10c, E=1.05, $X_d'=0.075$, $X_\ell=0.05$, $X_g=0.025$, $B_f=0.48$, $V_f^\star=1.0$, $I_{\rm mx}=2.0$, $I_{\rm m,opr}=1.0$, and $\tau_{\rm rly}=10\,{\rm s}$. The calculation of the currents I_m^{\diamond} and I_m^{\diamond} for Fig. 10c follow. The value of Z_m is from Fig. 11; its calculation for any ω_m is in Section V-B.

In Fig. 10a, the SPIM current when powered by an IBR is:

$$\widetilde{I}_m^{\diamond} = \frac{1}{1 + jB_f(jX_q + jX_\ell + Z_m)} \widetilde{I}_f \tag{40}$$

where $\widetilde{I}_f = \min\{I_f^*, I_{mx}\} \angle \phi_f$ is from the current command:

$$I_f^* \angle \phi_f = \frac{j B_f(j X_g + j X_\ell + Z_m) + 1}{j X_g + j X_\ell + Z_m} \widetilde{V}_f^*$$
 (41)

for $\widetilde{V}_f^* = V_f^* \angle 0^\circ$. Here, V_f^* and $I_{\rm mx}$ are respectively the IBR voltage set-point and its rated current. To the Authors' understanding, (40) and (41) have not been posed in the literature for analysis of thermal relays because they are a consequence of Section II-A. The parameter X_ℓ encapsulates the reactances of transformers and transmission lines and Z_m models the impedance of the SPIM.

From (40)–(41), the rms voltage magnitude of:

$$\widetilde{V}_f = (jX_g + jX_\ell + Z_m)\widetilde{I}_m^{\diamond} \tag{42}$$

in Fig. 10a is maintained at V_f^{\star} only if $I_f^{\star} \leq I_{\text{mx}}$ as a result of the voltage regulator with current limiter discussed in Section II-A. Otherwise, the voltage magnitude of (42) drops because of (40) and (41). In this paper, $\widetilde{I}_m^{\diamond}$ of (40) and Fig. 10a is contrasted against the one in Fig. 10b:

$$\widetilde{I}_{m}^{\triangleleft} = \frac{\widetilde{E}}{jX_{d}' + jX_{\ell} + Z_{m}}$$

$$\tag{43}$$

with $\widetilde{E} = E \angle 0^{\circ}$ the voltage behind a transient reactance, X'_d , of a classical synchronous machine model [7].

B. Asymmetrical Motor Impedance

The impedance Z_m of an asymmetrical motor with start-run capacitor for (40)–(43) as function of ω_m of (27) is:

$$Z_m(\omega_m) = \frac{\widetilde{V}_{sm}}{\widetilde{I}_{sm} + \widetilde{I}_{sa}} \tag{44}$$

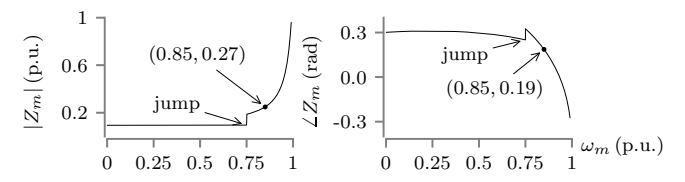
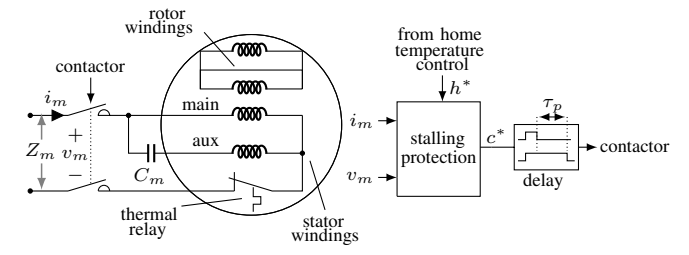


Fig. 11. Impedance vs. rotor speed of an asymmetrical single-phase motor.



(a) AC-compressor motor wiring

(b) stalling protection

Fig. 12. A/C-compressor motor including a two-pole contactor, a thermal relay, start-run capacitor $C_m \in \{C_{\text{run}}, C_{\text{start}} + C_{\text{run}}\}$, and proposed protection.

where the currents \widetilde{I}_{sm} and $\widetilde{I}_{sa} = N_{ma}\widetilde{I}'_{sa}$ respectively model the main and auxiliary winding ones (q.v. Fig. 12a) and meet:

$$\begin{bmatrix} \widetilde{V}_{sm} \\ \widetilde{V}'_{sa} \end{bmatrix} = \begin{bmatrix} Z_{11}(\omega_m) & Z_{12}(\omega_m) \\ Z_{21}(\omega_m) & Z_{22}(\omega_m) \end{bmatrix} \begin{bmatrix} \widetilde{I}_{sm} \\ \widetilde{I}'_{sa} \end{bmatrix} . \tag{45}$$

The entries of this 2-by-2 matrix derive by studying in the frequency domain the two-axis circuit of [52, Fig. 3]. The entry $Z_{22}(\omega_m)$ encapsulates the switching of C_m in Fig. 12a for start $C_m = C_{\rm start} + C_{\rm run}$ if $\omega_m < 0.75$ p.u. and run $C_m = C_{\rm run}$ if $\omega_m \geq 0.75$ p.u. In (44) and (45), $\tilde{V}'_{sa} = N_{ma}\tilde{V}_{sm}$ and $\tilde{V}_{sm} = V_{m,{\rm rtd}} \angle 0^\circ$ where $N_{ma} = N_m/N_a$ is the main-to-auxiliary winding turn ratio and $V_{m,{\rm rtd}}$ is the rms rated voltage. Figure 11 illustrates the magnitude and angle of the SPIM impedance with start-run capacitors vs. rotor speed. The SPIM and capacitor parameters are from Table III in Section VI. There, $|Z_m|$ is relatively low even if $\omega_m = 0.85$ p.u. The $|Z_m|$ and $\angle Z_m$ jump at $\omega_m = 0.75$ p.u. is because $C_m : C_{\rm run} \to C_{\rm start} + C_{\rm run}$ [q.v. C_m in Fig. 12] when $d\omega_m/dt < 0$.

C. Proposed Electronic Stalling Protection

An electronic approach is proposed to disconnect a stalled SPIM powered by IBRs before under-voltage load shedding relays disconnect a complete feeder [11]. In Fig. 12b, the principle is to open the contactor when the SPIM impedance is relatively low *and* its rotor is decelerating.⁶ The novelty is that deceleration is estimated from impedance which is feasible only if impedance is monotonically increasing on rotor speed.

The estimated SPIM impedance with start-run capacitor is:

$$\left| \widetilde{Z}_m \right| = \frac{\sqrt{\phi_v}}{\sqrt{\phi_i} + \epsilon} \text{ where}$$
 (46)

$$\frac{d}{dt}\phi_v=\frac{1}{\tau_c}\left(-\phi_v+v_m^2\right) \text{ and } \frac{d}{dt}\phi_i=\frac{1}{\tau_c}\left(-\phi_i+i_m^2\right) \ . \ (47)$$

The respective states ϕ_v and ϕ_i serve to filter the squares of the time-domain values of v_m and i_m in Fig. 12a. The time constant $\tau_c = 10/\omega_b$ where ω_b is the rated electrical angular

⁶Contactors automatically open when rms voltage drops below 35%. If the voltage is higher than 50%, the contactor is likely to remain closed [15].

frequency. The parameter ϵ in (46) is a relatively small value to prevent division by zero when $i_m(t) = 0$.

To determine whether the rotor is decelerating, e.g., after a fault, consider the indicator function $\mathscr{I}: \mathbb{R} \mapsto \mathbb{R}$:

$$\mathscr{I}(d\widetilde{\omega}_m/dt) = \begin{cases} 1 & \text{if } d\widetilde{\omega}_m/dt < -\epsilon_{\omega} \\ 0 & \text{otherwise} \end{cases}$$
 (48)

$$\frac{d}{dt}\widetilde{\omega}_{m} = \frac{1}{\tau_{f}} \left(-\widetilde{\omega}_{m} + \omega_{m}^{\dagger} \right) \text{ with } \omega_{m}^{\dagger} = \mathcal{L} \left(\left| \widetilde{Z}_{m} \right| \right)$$
 (49)

where $\epsilon_{\omega} > 0$ is a small parameter and $\widetilde{\omega}_m$ is the filtered version of the estimated rotor speed, ω_m^{\dagger} , which is obtained from $\left|\widetilde{Z}_m\right|$ of (46) via (49). In (49), $\mathcal{L}: \mathcal{Z} \mapsto \Omega$ is a lookup table that is constructed offline from calculated coordinated pairs $(|Z_m|, \omega_m)$, q.v. Section V-B. Ascertaining acceleration/deceleration is possible only if $|Z_m|$ is monotonically increasing on ω_m which applies here, q.v. Fig. 11. Otherwise, deceleration could be wrongly determined.

Lemma 1: $d|Z_m|/dt \neq 0$ and $d\omega_m/dt \neq 0$ have the same signs only if $|Z_m|$ is monotonically increasing on ω_m .

Proof: From the chain rule of time-domain quantities:

$$\frac{d|Z_m|}{dt} = \frac{d|Z_m|}{d\omega_m} \frac{d\omega_m}{dt}$$
 (50)

the time-derivative signs are equal only if $d |Z_m|/d\omega_m > 0$.

The stalling protection of Fig. 12b steers the status of the two-pole contactor in Fig. 12a via the following command:

$$c^* = \begin{cases} 0 & \text{if } \left| \widetilde{Z}_m \right| < \left| Z_m \right|^* \text{ and } \mathscr{I}(d\widetilde{\omega}/dt) = 1 \\ h^* & \text{otherwise.} \end{cases}$$
 (51)

The contactor is open when $c^*=0$ and closed if $c^*=1$. The parameter $|Z_m|^*$ in (51) is a minimum permissible motor impedance when the rotor is *decelerating*. Please, recall from (49) that $\mathscr{I}(d\widetilde{\omega_m}/dt)$ of (48) can be determined from impedance as long as Lemma 1 holds. The command c^* of (51) is delayed by τ_p seconds in Fig. 12b using a binary off delay for relay coordination proposes. Motors that are electrically far from a substation may be set to trip faster than closer ones. During normal operation, c^* of (51) follows the command, $h^* \in \{0,1\}$, from a home controller, q.v. Fig. 12b.

VI. CASE STUDIES

The dynamic performance of two hybrid PV power plants energizing the 13.8-kV radial feeder in Fig. 2 is analyzed via four case studies. Each power plant of Fig. 2 is assumed to have four 2.5-MVA/0.69-kV IBRs along with a 0.69/34.5 kV step-up transformer as shown in Fig. 1. A 20-MVA IBR capacity was necessary to successfully energize all the SPIMs of Fig. 2. A lower MVA capacity did not yield enough startup currents to energize all the SPIM clusters. The dclink of each IBR is powered by a 2.0-MW PV array and a 2.0-MWh BES. The first case study shows restoration performance under varying solar irradiance. The second and third case studies demonstrate the performance of the realistic compressor model in Section IV, the classical thermal relay in Section V-A, and the proposed electronic stalling protection

TABLE I
TIMED CIRCUIT BREAKER EVENTS FOR FIG. 2

breaker	H1	H2	C1	H3	H4	C2	C3	C4	C5	C6	C7	
t_c (s)	5	5.5	7	7.5	8	10	13	16	19	22	25	Г
t_o (s)	-	-	-	33.15	33.15	-	-	-	-	-	-	Г

TABLE II PARAMETERS OF A HYBRID PV INVERTER AND ITS CONTROLS

par.	values	units	par.	values	units	par.	values	units	par.	values	units
$\overline{C_{dc}}$	64.3	mF	r_f	6.0	$m\Omega$	L_f	0.1515	mΗ	C_f	0.9	mF
κ_{dc}	40	A/kJ	τ_{dc}	10	ms	$v_{ m mn}$	1.2	kV	κ_{ω}	0.05	p.u.
$ au_e$	5.3	ms	τ_p	40	ms	$ k_f $	1	p.u.	$ au_f $	7.3	ms
κ_v	0.54	A/V	τ_v	20	ms	κ_i	0.3				
$ au_l$	0.54	ms	$ au_{ m sw}$	2	ms	\overline{s}_c	95	%	\underline{s}_c	10	%
C_l	10	μ F	L_l	0.1	mΗ	r_l	15.7	$m\Omega$	τ_d	2	μ s
κ_b	0.038	1/A	$ au_b$	2	ms	\bar{i}_l	3.5	kA	\underline{i}_l	-3.5	kA

in Section V-C during FIDVR instances because of a fault in the 138-kV transmission circuit, q.v. Fig. 2. The fourth case study compares the dynamic performance of the thermal and electronic protections when the system of Fig. 2 is powered by synchronous machines. The sequential times when the breakers of Fig. 2 close, t_c , and open, t_o , are in Table I. The power plants energize their Δ -Yg transformers at $t=2.5\,\mathrm{s}$.

These studies are conducted via a detailed EMT model of Fig. 2 which was implemented on PSCAD v5.0. The PSCAD simulations, using a $5 \mu s$ time step, were conducted on a desktop with 32 GB of RAM and a four-core 3.5-GHz Intel® Xeon® i3 processor. The time to simulate 45 s of reality was 44 min ca. The optimal set-point v_{dc}^* from Section III-A is computed using a custom FORTRAN script which is executed every 50 ms in PSCAD. As explained in Section II-B, only one inverter out of four is simulated at each power plant, its current outputs are scaled up by a factor of four. This is done here via the standard PSCAD scaling component [48] which considers 2.5% series impedance with respect to the 2.5-MVA inverter rating at the 34.5-kV side. In Fig. 2, the PV power plants are connected to the distribution feeder via two 138kV sub-transmission lines and represented with frequencydependent models [62]. Each distribution line of Fig. 2, e.g., the one connecting buses '0' and '1,' is modeled using a Π section as in [28]. The physical and control parameters of the PV subsystem in Fig. 1 are in Table II. Table III reports the parameters of the reciprocating compressor in Fig. 8 and the SPIM parameters. The SPIM is rated for 4.524 kW, 230 Vrms, and 60 Hz; the parameters are scaled from the ones explained in [52], [63]. The compressor model is implemented via a custom FORTRAN script in PSCAD.

A. Case I: Restoration Under Varying Solar Irradiance

The restoration of Fig. 2 is conducted as in Section II-B. It considers the realistic compressor model in Section IV-B because the behavioral model is not suited to represent SPIM acceleration, q.v. Section IV-A. The results of this case study are reported in Figs. 13–17. Figure 13 illustrates the dynamic performance of one hybrid GFM IBR as the one in Fig. 1 during step-wise variations of solar irradiance, I_r , in per unit of 1,000 W/m². In particular, one can learn from Fig. 13 that: (A) I_r steps up from 0.5 to 1.0 at t = 10.0 s, then drops to

TABLE III COMPRESSOR AND SPIM PARAMETERS

	compressor [59]			SPIM	
par.	values	units	par.	values	units
r_s	0.01	m	r_r	0.74	Ω
r_p	0.022	m	$X_{\ell r}$	0.38	Ω
ℓ	0.095	m	r_{sm}	0.36	Ω
p_s	0.47/68	MPa/psi	$X_{\ell sm}$	0.50	Ω
p_d	1.034/150	MPa/psi	r_{sa}	0.91	Ω
\mathcal{V}_1	6.55×10^{-5}	m^3	$X_{\ell sa}$	0.41	Ω
\mathcal{V}_2	2.95×10^{-5}	m^3	X_m	11.88	Ω
\mathcal{V}_3	4.91×10^{-6}	m^3	$C_{ m start}$	860	$\mu \mathrm{F}$
\mathcal{V}_4	1.03×10^{-5}	m^3	C_{run}	200	μ F
D_f	500	Ns/m	N_{ma}	1/1.18	-
D_p	0.3	Ns ² /m	J	0.0022	$kg \cdot m^2$

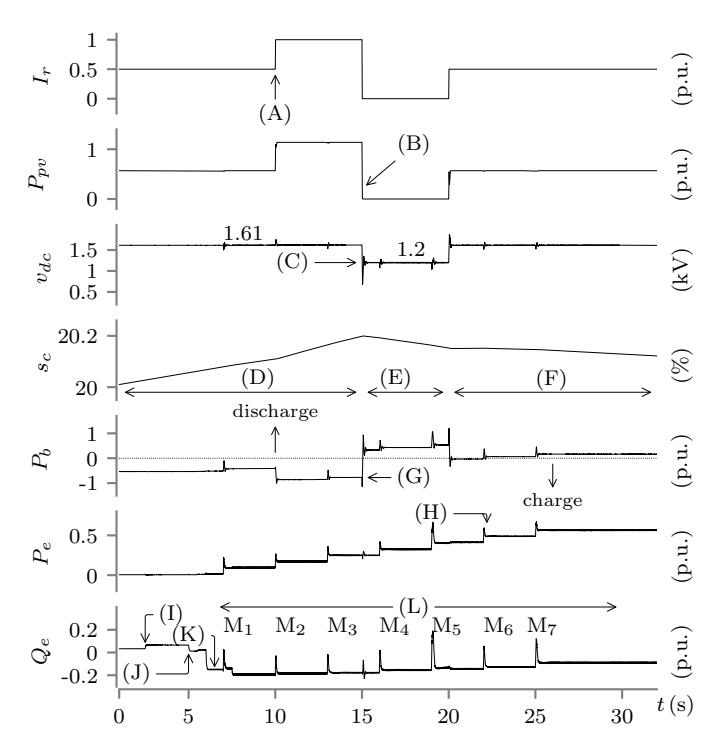


Fig. 13. Case I: Performance of one IBR as in Fig. 1 during restoration.

0.0 at $t = 15.0 \,\mathrm{s}$ to challenge control of the hybrid system. (B) At t = 15.0 s, the PV-array power $P_{pv} \rightarrow 0$ p.u. because $I_r \rightarrow 0$. (C) The dc-link voltage drops from 1.6 kV to 0.68 kV and then recovers to $v_{\rm mn}=1.2\,{\rm kV}$ as a consequence of (B); recall $v_{\rm mn}$ is defined in Section III-B. (D) The battery SoC, s_c , increases because $P_{pv} > P_e$ for $t \in [0, 15]$ s, q.v. Section III. (E) s_c decreases because $P_{pv} < P_e$ for $t \in (15, 20]$ s. (F) s_c is almost constant because $P_{pv} \approx P_e$ for $t \in (20, 30]$ s. (G) Battery power [q.v. Fig. 1] changes at $t = 15.0 \,\mathrm{s}$ from $P_b = -0.8 \,\mathrm{p.u.}$ charging [buck mode in Section III-C] to $P_b = 0.4 \,\mathrm{p.u.}$ discharging [boost mode] because of (B). (H) The short-lived overshoots in ac power P_e [q.v. Fig. 1] are because of the start-up of SPIMs. (I) Reactive power Q_e from Fig. 1 slightly increases to 0.064 p.u because the 10-MVA 34.5/138-kV Δ -Y_g transformers of Fig. 2 are energized. (J) Q_e drops at $t = 5.0 \,\mathrm{s}$ because one transmission branch is energized, q.v. Fig. 2, and Table I. (K) Q_e decreases to -0.15 p.u. because the distribution feeder of Fig. 2, having

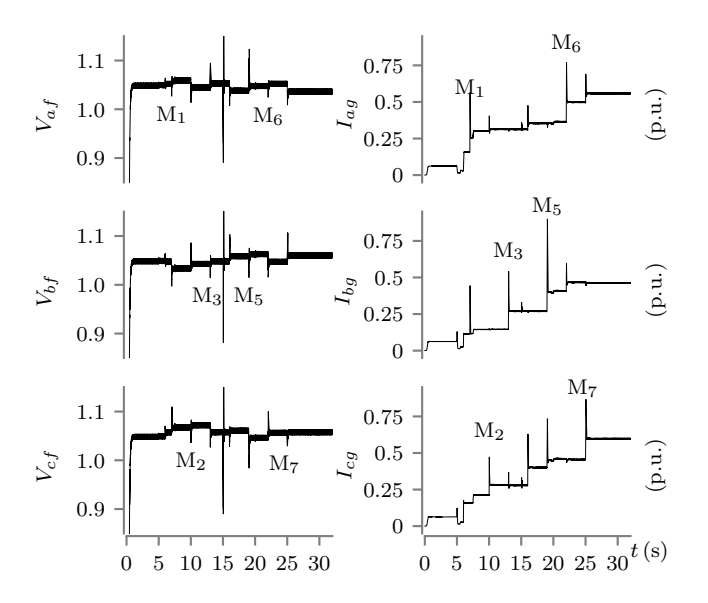


Fig. 14. Case I: Performance of rms line-to-ground voltages and phase currents of one IBR during restoration.

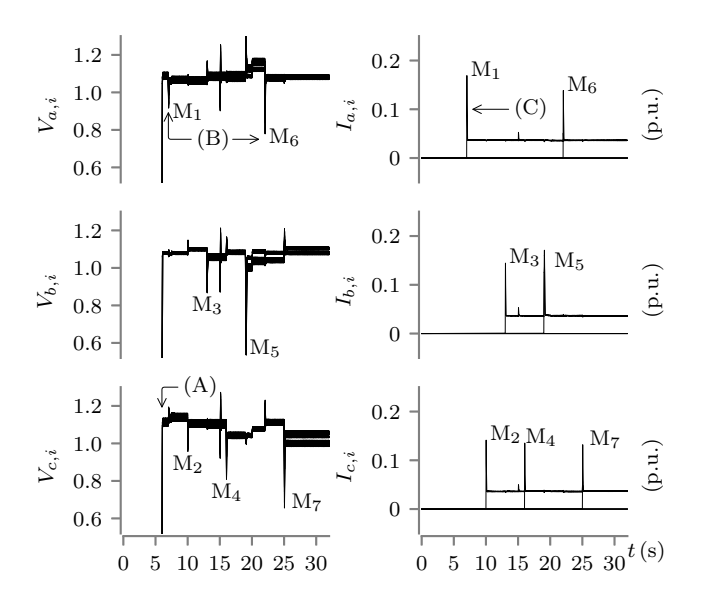


Fig. 15. Case I: Behavior of rms voltages and currents at the 13.8-kV distribution feeder nodes of Fig. 2.

several capacitor banks, is energized at $t=6.0\,\mathrm{s}$. (L) Q_e momentarily increases and then decreases because of the starting up of SPIM clusters $\mathrm{M_1-M_7}$. To complement Fig. 13, Fig. 14 reports line-to-ground rms voltages, V_{af} , V_{bf} , and V_{cf} , that are measured at capacitors of the LC filter in Fig. 1. It also reports the phase currents I_{ag} , I_{bg} , and I_{cg} which correspond to the $0.69\,\mathrm{kV}$ -side of the XFMR in Fig. 1. The quantities in Fig. 14 have been normalized with respect to the ratings of the GSI, i.e., $2.5\,\mathrm{MVA}$ and $0.69\,\mathrm{kV}$. In Fig. 14, IBR rms voltages momentarily drop while current rises because of the starting up of SPIM motor clusters $\mathrm{M_1-M_7}$. The voltage transients by $t=15.0\,\mathrm{s}$ are because of the sudden drop in solar irradiance that leads to momentary low dc-link voltage.

The behaviors of voltages, currents, motor speeds, and OLTC at the feeder buses of Fig. 2 during the restoration are

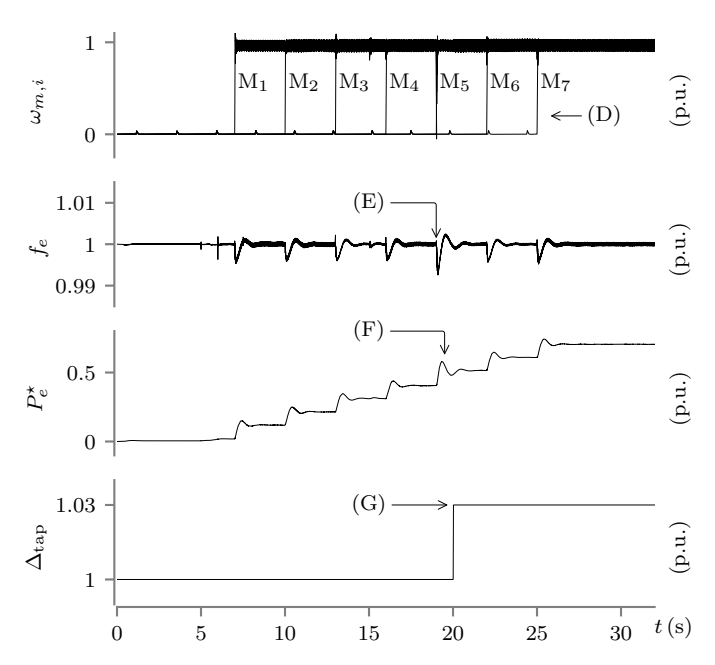


Fig. 16. Case I: Behavior of motor speed, grid frequency, power set-point, and OLTC tap of Fig. 2 during the restoration.

reported in Figs. 15 and 16. In Fig. 15, each $V_{x,i}$ and $I_{x,i}$ with $x \in \{a, b, c\}$ and $i \in \{0, 1, 2, \dots, 7\}$ are: (i) the rms singlephase voltage observed at the i-th 13.8-kV bus and (ii) rms single-phase current flowing into the SPIM and resistive load cluster, e.g., V_3 and I_3 in Fig. 2 is by the load connected to phase 'b' (or ϕ_b). In Fig. 16, each per-unit rotor speed $\omega_{m,i}$ corresponds to one machine within the M_i motor cluster of Fig. 2. In Figs. 15 and 16, one can learn that: (A) The rms phase voltages V_1 – V_7 are as high as 1.08 p.u. when the feeder energizes because of the feeder capacitors. (B) The voltage dips for each M_i is because of the SPIM start-up current. (C) The start-up current of SPIM cluster M_1 , for example, is a high as 0.17 p.u. (1.0-kA/13.8-kV bases) which contrasts its steady state current of 0.04 p.u. (D) The rotor speed of one motor in cluster M7 rises from stand still as fast as the motors in the other clusters. (E) The frequency, f_e , drops from 1.0 p.u. of 60 Hz to 0.995 p.u. at t = 19 s because of SPIM M_5 acceleration, then it returns to rated because of the frequency controller, q.v. Fig. 3d. The fast transients of f_e , e.g., by $t = 5.0 \,\mathrm{s}$, are because of transmission-line energization. (F) The frequency control command P_e^{\star} of Fig. 3d changes to compensate frequency deviations because of SPIM start-up. (G) The OLTC tap increases to 1.03 p.u. to compensate for the voltage drop at node '0' of Fig. 2 as a result of significant load increase.

Figure 17 reports the physical variables of one compressor in M_7 , q.v. Section IV. During start-up, the compressor changes its piston position x, pressure p, and volume \mathcal{V} because T_e of (27) accelerates the rotor of the SPIM.

B. Case II: FIDVR Event with Realistic Compressor

This study contrasts the performance of Fig. 2 when the compressors are represented via: (i) the realistic model in Section IV-B and (ii) the behavioral one in Section IV-A.

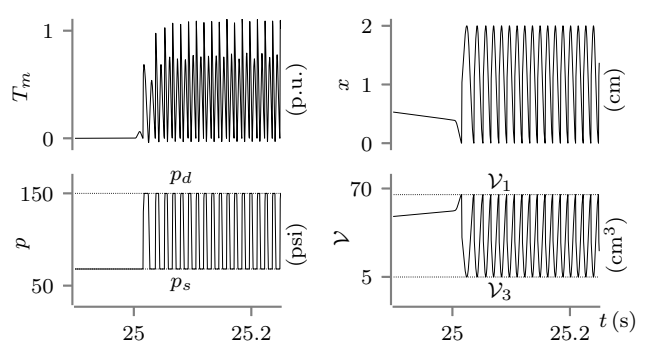


Fig. 17. Case I: Behavior of a realistic compressor during M7 cluster start-up.

Recall that Table III reports the parameters of the realistic compressor model. The behavioral parameters for (28) are $k_{\rm av}=0.25$ and $k_{\rm av}=0.75$ in p.u. of the compressor rating which are scaled from [28, Table III]. The simulation times using the realistic and behavioral compressor models were approximately 44 minutes and 43 minutes, respectively. This is indicative that the realistic compressor model of Section IV-B is computationally light. The FIDVR event is triggered by a fault between phase 'c' and ground at the middle of the line between the breakers H3 and H4 in Fig. 2. The SPIMs are equipped with thermal relays having $\tau_{\rm rly}=10.0\,{\rm s}$ and $I_{m,{\rm rly}}=2.0\,{\rm p.u.}$ in its SPIM base, q.v. Section V-A. The results are reported in Figs. 18–22.

One can learn from Figs. 18 and 19 that: (A) The voltage magnitude of every phase decreases because of IBR limited current ratings. (B) The realistic compressor model leads to voltage recovery at $t = 35.5 \,\mathrm{s}$ whereas the behavioral counterpart at $t = 37.0 \,\mathrm{s}$ because they develop different mechanical torques. (C) Current withdrawn by the SPIMs driving the behavioral compressor model can be higher than when driving the realistic one. Figure 20 shows that: (A) After stalling, the SPIMs that drive the realistic compressor successfully re-accelerate clusters M1, M4, M5, M7; when the SPIMs drive the behavioral compressor model only clusters M_4, M_5, M_7 recover. (B) The per-unit temperature Θ of motor M₇ using realistic compressor model is slightly higher due to the longer start-up time, q.v. Fig. 16. In contrast, when using the behavioral model, the temperature of all motors is relatively low because the compressor is disconnected during startup [27, p. 26–27]. The motors trip when Θ reaches $\Theta^* =$ 1.0 p.u. Notably, the speed recovery when using the realistic compressor model is different from that of the behavioral one. This is because the behavioral model is not suited to capture motor acceleration or re-acceleration, q.v. Section IV-A.

Figure 21 reports the mechanical and electrical torques of one motor within the cluster M_5 . The realistic T_m resembles a combination of sinusoidal waveforms (q.v. Section IV-B) whereas the behavioral T_m is a triangular waveform. Notably, the electromagnetic torque T_e is different for the realistic and behavioral cases as depending on rotor speed and position which is impacted by T_m , q.v. (27).

Figure 22, on the other hand, reports electrical quantities at the terminals of one GSI of Fig. 1 in per-unit with respect to the GSI rating. In Fig. 22: (A) After the fault at $t = 33.0 \,\mathrm{s}$,

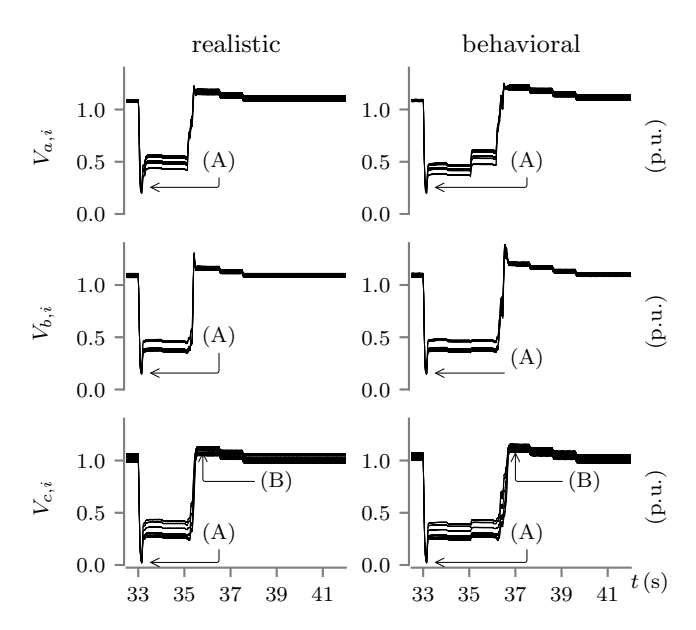


Fig. 18. Case II: Line-to-ground rms voltages of feeder nodes during FIDVR events using the realistic and behavioral compressor models.

the instantaneous currents, i_{cf} , can be as high as 1.39 p.u., then it is driven towards 1.0 p.u. by the current regulator of Fig. 3b. Note here that the GSI currents are not precisely bounded at 1.0 p.u. because the current regulator has a settling time of 5 ms which limits ideal control during asymmetrical faults. However, the identified trespassing is short lived and perhaps inoffensive to the IGBTs when studying their thermal behaviors as suggested in [37]. A simulation without the antiwindups yielded currents as high as 4.5 times of the GSI rated current which would have destroyed its semiconductors. (B) Because of the current limiting, the magnitude of the IBR voltage waveforms are below rated. (C) The voltage waveforms do not recover to their rated values after the fault is cleared at $t = 33.15 \,\mathrm{s}$ because of motor stalling and GFM current limiters. (D) The speed, ω_c in Fig. 3c, increases to $1.035 \,\mathrm{p.u.}$ during the fault event because P_e and P_e reduces, q.v. (6). (E) The variation of dc-link voltage, v_{dc} in Fig. 1, is minor which elucidates the desired control performance of Sections III-B and III-C. (F) Active power, P_e , drops from 0.58 p.u. to 0.07 p.u. and oscillates because the line-to-ground fault (phase 'c') which blocks power transfer to the feeder. (G) Reactive power, Q_e , automatically rises from 0.16 p.u. to 0.42 p.u. after the fault in phase 'c' is cleared because the IBR controls of Section II-A are engineered to regulate terminal voltages which remain relatively low during the FIDVR event, hence currents are steered to rated values.

Overall this case study has showcased: (i) The ability of the hybrid PV grid-forming power plants to ride through faults which is helpful to address FERC order 2023 [43, pp. 1081–1099]. And (ii) the capability of these power plants to withstand sustained low voltages events which can be useful to address NERC PRC-024-3 requirements [44]. This capabilities are critical to not disconnect IBRs, otherwise, they can jeopardize the reliability of power grids.

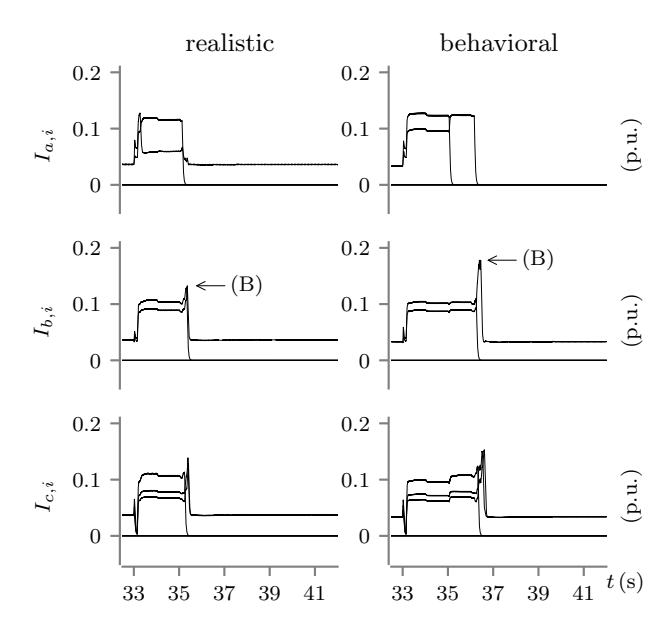


Fig. 19. Case II: Three-phase rms currents during FIDVR events using the realistic and behavioral compressor models.

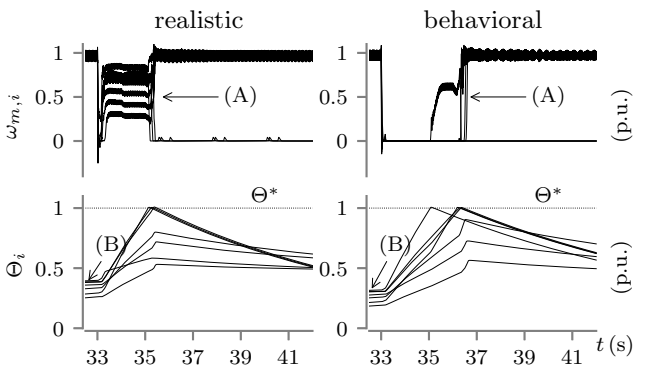


Fig. 20. Case II: Speed and temperature for FIDVR events using the realistic and behavioral compressor models.

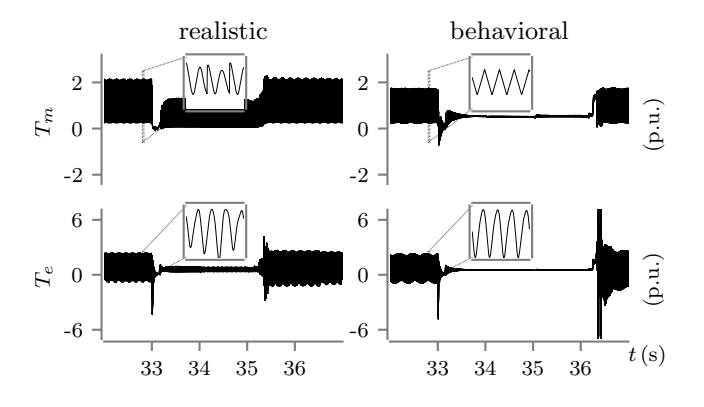


Fig. 21. Case II: Torque of M_5 FIDVR events using the realistic and behavioral compressor models.

C. Case III: FIDVR Event with Electronic Protection

This subsection contrasts the response of the electronic protection in Section V-C against the thermal relay in Section V-A. It also considers the realistic compressor model in Section IV-B during a FIDVR event. Here, $\epsilon_{\omega}=0.01$

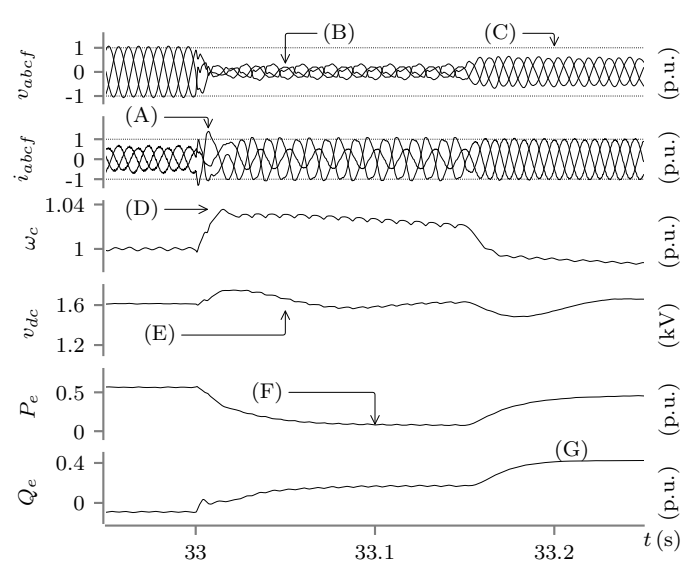


Fig. 22. Case II: Per-unit inverter voltages $(v_{abf}, v_{bcf}, v_{caf})$, currents (i_{af}, i_{bf}, i_{cf}) , droop-controlled speed (ω_c) , dc-link voltage (v_{dc}) , active power (P_e) , and reactive power (Q_e) during the fault. The straight dotted lines represent rated ac values.

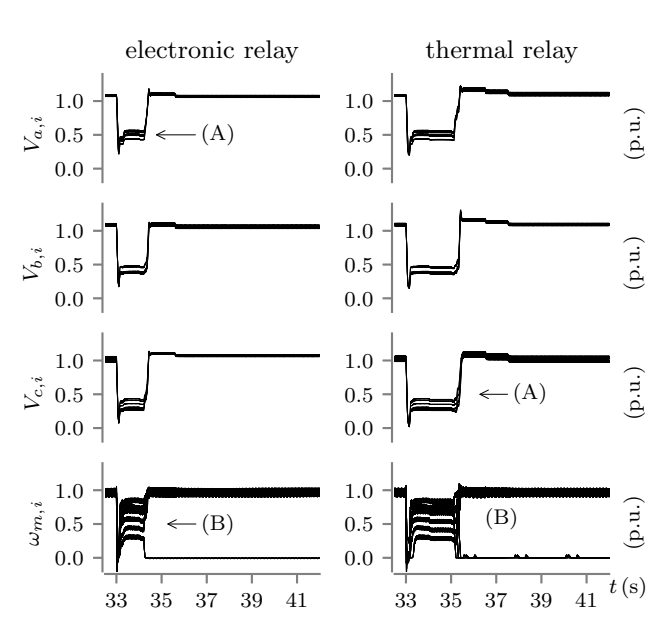


Fig. 23. Case III: FIDVR performance using electronic and thermal relays.

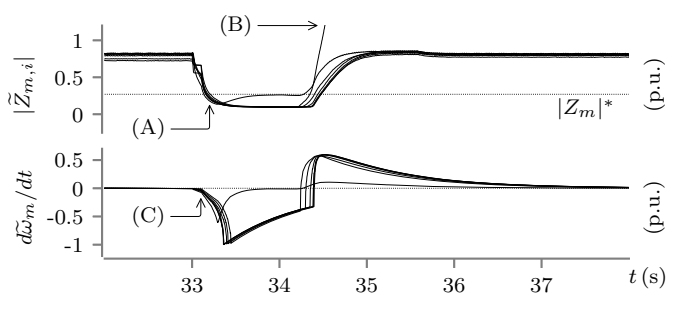


Fig. 24. Case III: Estimated impedance and rotor deceleration/acceleration.

for (48) and each off-delay time $\tau_{p,i} = 1.0 + 0.25 \cdot (7 - i)$, $i = 1, 2, \ldots, 7$ (q.v. τ_p in Fig. 12b) are used in each M_i motor cluster of Fig. 2. This delay is judiciously selected so that, for

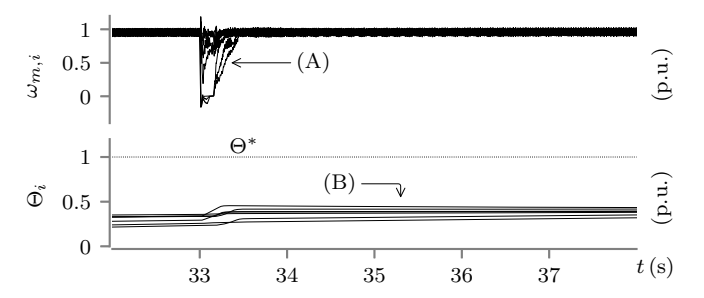


Fig. 25. Case IV: FIDVR performance using synchronous machines and SPIM thermal protection.

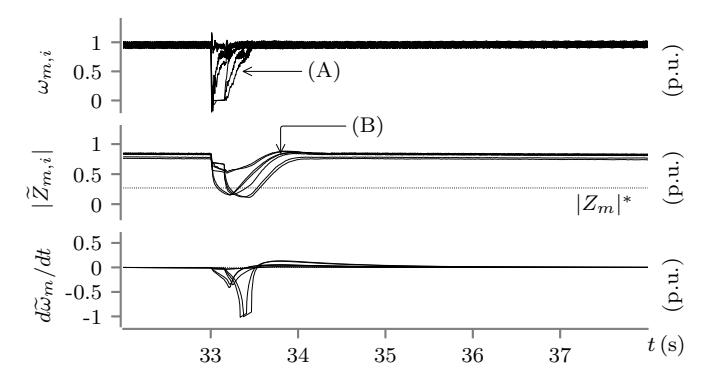


Fig. 26. Case IV: FIDVR performance using synchronous machines and SPIM electronic protection.

example, the 6-th motor cluster trips after $0.25\,\mathrm{s}$ of the 7-th one if stalling happens in both clusters; note that M_7 is at the feeder tail, hence coordinated for relatively fast tripping.

The results of this case are in Figs. 23 and 24. Figure 23 reports that: (A) The electronic relay leads to voltage recovery at t = 35.0 whereas the thermal-relay counterpart at t = 37.5 s because electronic approach does not require heating for tripping. (B) When using the electronic protection, the rotor speed of clusters M₁-M₆ recover. In contrast, only clusters M₁, M₄, M₅, M₇ speeds recover when using the thermal relay. In Fig. 24, one can recognize that: (A) The estimated impedance $|\widetilde{Z}_{m,i}|$ via (46) is lower than the set-point $|Z_m|^* =$ $0.27 \,\mathrm{p.u.}$ (dotted line) for (51) after the fault at $t=33.0 \,\mathrm{s}$ because the SPIM speeds are decreasing. (B) The impedances of the SPIM clusters that have tripped (M₇) are relatively large which is expected, q.v. (46). (C) Deceleration is correctly estimated on all motors after $t = 33.0 \,\mathrm{s}$ which enables SPIM tripping during the FIDVR event. Recall that low-impedance and deceleration command SPIM tripping after the off-delay time $\tau_{p,i}$ has elapsed, q.v. (51) and Fig. 12b. Overall, the electronic relays contributed to the recovery of six SPIM clusters, i.e., $6 \times 177 = 1062$ A/C units, q.v. Fig. 2. In contrast, the thermal relay supported the speed recovery of only four

D. Case IV: Synchronous Machine Benchmark

SPIM clusters, i.e., $4 \times 177 = 708$ A/C units.

This case study compares the dynamic performance of the thermal relay and electronic stalling protection when the system in Fig. 2 is powered by two synchronous generating sets. We also compare the response of synchronous machines

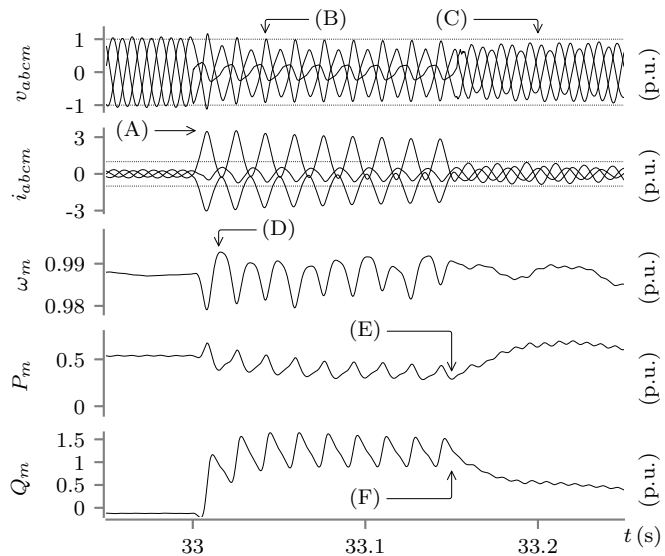


Fig. 27. Case IV: Per-unit machine voltages $(v_{abm}, v_{bcm}, v_{cam})$, currents (i_{am}, i_{bm}, i_{cm}) , rotor speed (ω_m) , as well as machine active (P_m) and reactive (Q_m) power during and after the fault. The straight dotted lines represent rated values. Per unit values are given with respect to the machine MVA and voltage ratings.

against that of the IBRs. The FIDVR event is also triggered here by a fault between phase 'c' and ground at the middle of the line between the breakers H3 and H4 in Fig. 2; this to compare with observations from Section VI-B. In this case study, each 4×2.5 MVA hybrid power plant of Fig. 2 is substituted by one 10-MVA 13.8-kV synchronous machine driven by a hydroturbine. Hence, 10-MVA 13.8/138-kV Δ -Yg transformers are used in Fig. 2 in lieu of the 34.5/138-kV units. The results of this case study are reported in Figs. 25–27.

For the thermal relay case, we learn in Fig. 25 that: (A) The angular speeds of all SPIM clusters recover by $t=34.0\,\mathrm{s}$; clusters M_1 and M_6 did not face deceleration and other clusters speed recovered after stalling. This contrasts Fig. 23-B where SPIMs M_1 , M_2 , M_3 and M_6 stalled because their thermal relays activated. (B) Thermal relays corresponding to SPIM clusters do not reach their thermal limits, hence, they do not cause motor tripping. For the electronic relay case, one can deduce from Fig. 26 that: (A) The speed of all SPIM clusters recover by $t=34.0\,\mathrm{s}$. (B) Clusters M_1 and M_6 did not face deceleration and other clusters speed recovered after stalling. Overall, the thermal and proposed electronic relays have comparable behaviors when the power system is energized by synchronous machines. This is indicative that the electronic relay does not misoperate.

Finally, Fig. 27 elucidates that: (A) The fault currents supplied by one of the synchronous machines are more than three times its rated value and have notable dc-offsets. This observation contrasts Fig. 22-A in which IBR currents are limited to around 1.0 p.u. and seem to not have dc-offsets. (B) Line-to-line voltage v_{abm} does not significantly drop whereas v_{cam} and v_{bcm} significantly drop because the fault is between phase 'c' and ground. This behavior contrasts the observation in Fig. 22-B because of IBR current limits. (C) The machine voltages do not recover to their rated values after the fault is cleared at $t=33.15\,\mathrm{s}$ because of motor stalling and voltage

regulator limits which also happened in Fig. 22-C. (D) The rotor speed of the machine, ω_m , stays around 0.99 p.u. during and after the fault because of inertia; secondary frequency control was also considered. This contrast to the behavior of ω_c in Fig. 22-D which increased because of the absence of inertia. (E) The machine active power, P_m , drops from 0.5 p.u. to 0.28 p.u. and oscillates because the line-to-ground fault (phase 'c'); in Fig. 22-F power dropped to 0.07 p.u. (F) Reactive power, Q_m , automatically rises from -0.21 p.u to 1.63 p.u. after the fault in phase 'c' is cleared. The reason is that the machine voltage regulator increases excitation current in an attempt to maintain machine terminal voltages at rated during the FIDVR event. In Fig. 22-G, Q_e increased because the grid-forming controller boosted GSI currents (within limits) to try to maintain capacitor voltages at rated.

VII. CONCLUSION

This paper has engineered the technology for hybrid GFM IBRs so that they can: (i) optimally transfer power from a de-coupled photovoltaic array and battery into an ac grid during restoration and (ii) withstand FIDVR events because of SPIM stalling. To that end, it was engineered in Section III-B anti-windup proportional-integral (PI) regulators to optimally charge and discharge the BES. It was shown in Section VI-A that the controller performs well under varying solar irradiance during restoration. In Section IV-B, it was also derived a realistic compressor model for EMT studies of FIDVR events of grids with GFM IBRs and residential A/C units. This model is as computationally-light as the behavioral model of [27]-[29]. The key benefit is that the developed model can be used to study in the EMT domain both SPIM acceleration, deceleration, and re-acceleration which can happen during restoration and FIDVR events. In Section VI-B, the realistic compressor model contrasts the performance of the behavioral representation discussed in Section IV-A. This realistic model is critical to generate the right information to aid power system planners to make the right decisions.

In Section V-A, it was shown that IBR current limitations would delay the tripping of SPIM thermal relays which implied longer FIDVR events. Hence, an electronic protection was set forth in Section V-C to disconnect stalled SPIMs by estimating impedance and rotor deceleration. It was showcased in Section VI-C that several A/C units can recover when using the electronic relay. In Section VI-D, the electronic protection proved to perform as well as the thermal protection when the distribution grid is powered by synchronous machines. Remarkably, the proposed relay is helpful to prevent deenergizing an entire distribution feeder which can impact several neighborhoods by the selective disconnection of stalled motors. Although not done here, the functionality of the thermal relay can be also implemented within the electronic relay to protect SPIMs from internal faults, e.g., SPIM winding failures.

Overall, the developments and analyses of Sections II–VI can be useful to understand via EMT simulations the realistic performance of transmission-connected hybrid PV power plants during restoration and FIDVR events involving SPIMs

and residential A/C compressors [31]. Also, this paper can be used in the broad sense to address FERC order 2023 [43, pp. 1081–1099] and NERC PRC-024-3 requirements [44] because the proposed hybrid PV plant can reliably ride through faults and withstand FIDVR events.

Future work will address hybrid configurations including wind and hydrogen fuel cells and FIDVR co-simulation in the EMT and phasor domains. The discrepancy in reactive power in Fig. 9 of Section IV-B will be tackled using model identification [64] to determine the parameters of the SPIM and start-run capacitors from experimental data. It is also of interest to model the performance of scroll compressors which are becoming popular [65]. Moreover, effects of ambient temperature on SPIM compressors could be of interest. Another line of future work is the sizing of hybrid IBRs to ensure restoration and resource adequacy of islanded distribution grids. In this vein, also cost-benefit analyses of the proposed technologies in this paper including grid-forming inverters as well as electronics relays are desirable to compare against other technologies, e.g., STATCOMs.

VIII. ACKNOWLEDGEMENTS

We thank the anonymous Referees for their comments and suggestions which helped improve this paper. We also thank Prof. V. Ajjarapu from Iowa State University for his technical discussions during the development of this work.

The views expressed in the article do not necessarily represent the views of the DOE or the U.S. Government. The U.S. Government retains and the publisher, by accepting the article for publication, acknowledges that the U.S. Government retains a nonexclusive, paid-up, irrevocable, worldwide license to publish or reproduce the published form of this work, or allow others to do so, for U.S. Government purposes.

REFERENCES

- [1] "Solar futures study," U.S. Dept. of Energy, Tech. Rep., Sep. 2021.
- [2] Lawrence Berkely Nat. Lab., Berkeley, CA, USA, Hybrid Power Plants: Status of Operating and Proposed Plants, 2022 Edition. (Aug. 18, 2022). Accessed: May. 12, 2023. [Online Video]. Available: https://www.youtube.com/watch?v=LYFi4Gx7OAQ.
- [3] Y. Lin et al., "Research roadmap on grid-forming inverters," Nat. Renewable Energy Lab., Tech. Rep. NREL/TP-5D00-73476, Nov. 2020.
- [4] —, "Pathways to the next-generation power system with inverter-based resources: Challenges and recommendations," *IEEE Electrific. Mag.*, vol. 10, no. 1, pp. 10–21, Mar. 2022.
- [5] "FERC-NERC-regional entity joint review of restoration and recovery plans: Blackstart resources availability," FERC and NERC, Tech. Rep., May 2018.
- [6] J. O'Brien et al., "Electric grid blackstart: Trends, challenges, and opportunities," Pacific Northwest Nat. Lab., Tech. Rep. PNNL-29118, Oct. 2020.
- [7] P. M. Anderson, C. Henville, R. Rifaat, B. Johnson, and S. Meliopoulos, Power System Protection, 3rd ed. New York, USA: Wiley-IEEE Press, 2022
- [8] "Technical Reference Document Dynamic Load Modeling," North American Electric Reliability Corporation, Tech. Rep., Dec. 2016. [Online]. Available: https://www.nerc.com/comm/ PC/LoadModelingTaskForceDL/Dynamic%20Load%20Modeling% 20Tech%20Ref%202016-11-14%20-%20FINAL.PDF
- [9] B. Williams, W. Schmus, and D. Dawson, "Transmission voltage recovery delayed by stalled air conditioner compressors," *IEEE Trans. Power Syst.*, vol. 7, no. 3, pp. 1173–1181, Aug. 1992.
- [10] C. Taylor, "Concepts of undervoltage load shedding for voltage stability," IEEE Trans. Power Del., vol. 7, no. 2, pp. 480–488, Apr. 1992.

- [11] D. Tziouvaras, "Relay performance during major system disturbances," in 60th Ann. Conf. Protective Relay Engineers, College Station, TX, USA, Mar. 27–29, 2007, pp. 251–270.
- [12] S. M. Halpin, K. A. Harley, R. A. Jones, and L. Y. Taylor, "Slope-permissive under-voltage load shed relay for delayed voltage recovery mitigation," *IEEE Trans. Power Syst.*, vol. 23, no. 3, pp. 1211–1216, Aug. 2008.
- [13] H. Bai and V. Ajjarapu, "A novel online load shedding strategy for mitigating fault-induced delayed voltage recovery," *IEEE Trans. Power Syst.*, vol. 26, no. 1, pp. 294–304, Feb. 2011.
- [14] L. Taylor and S.-M. Hsu, "Transmission voltage recovery following a fault event in the metro Atlanta area," in *Proc. IEEE Power Eng. Soc. Summer Meeting*, Seattle, WA, Jul. 16–20, 2000.
- [15] J. Kueck, D. Kosterev, J. Undrill, and J. Eto, "Voltage sag and recovery influence for modeling motor loads," in 2014 IEEE PES T&D Conf. and Expo., Chicago, IL, Apr. 14–17, 2014.
- [16] S. M. Hashemi, M. Sanaye-Pasand, and M. Abedini, "Under-impedance load shedding: a new preventive action against voltage instability," *IET Gen., Trans. & Distribution*, vol. 13, no. 2, pp. 201–208, Nov. 2019.
- [17] A. R. R. Matavalam and V. Ajjarapu, "PMU-based monitoring and mitigation of delayed voltage recovery using admittances," *IEEE Trans. Power Syst.*, vol. 34, no. 6, pp. 4451–4463, Nov. 2019.
- [18] Y. Dong *et al.*, "An emergency-demand-response based under speed load shedding scheme to improve short-term voltage stability," *IEEE Trans. Power Syst.*, vol. 32, no. 5, pp. 3726–3735, Sep. 2017.
- [19] B. Kroposki et al., "Achieving a 100% renewable grid: Operating electric power systems with extremely high levels of variable renewable energy," *IEEE Power Energy Mag.*, vol. 15, no. 2, pp. 61–73, Mar-Apr. 2017.
- [20] R. H. Lasseter, Z. Chen, and D. Pattabiraman, "Grid-forming inverters: A critical asset for the power grid," *IEEE Trans. Emerg. Sel. Topics Power Electron.*, vol. 8, no. 2, pp. 925–935, Dec. 2020.
- [21] J. Matevosyan et al., "A future with inverter-based resources: Finding strength from traditional weakness," *IEEE Power Energy Mag.*, vol. 19, no. 6, pp. 18–28, Nov-Dec. 2021.
- [22] B. Kroposki *et al.*, "UNIFI specification for grid-forming inverter-based resources-version 1," Tech. Rep. UNIFI-2022-2-1, Dec. 2022.
- [23] D. Venkatramanan et al., "Grid-forming inverter technology specifications: A review of research reports and roadmaps," Tech. Rep. UNIFI-2022-1-1, Nov. 2022.
- [24] R. Beall and B. McNary, "Nearly 90% of U.S. households used air conditioning in 2020." [Online]. Available: https://www.eia.gov/ todayinenergy/detail.php?id=52558
- [25] X. Quan et al., "Photovoltaic synchronous generator: Architecture and control strategy for a grid-forming PV energy system," IEEE Trans. Emerg. Sel. Topics Circuits Syst., vol. 8, no. 2, pp. 936–948, Jun. 2020.
- [26] F. Zhao et al., "Control interaction modeling and analysis of grid-forming battery energy storage system for offshore wind power plant," IEEE Trans. Power Syst., vol. 37, no. 1, pp. 497–507, Jan. 2022.
- [27] Y. Liu, "Modeling of air-conditioner compressor single phase induction motor for transient analysis," M.S. thesis, Dept. Elect. Eng., Arizona State University, Tempe, AZ, USA, 2012.
- [28] Y. Liu, V. Vittal, J. Undrill, and J. H. Eto, "Transient model of air-conditioner compressor single phase induction motor," *IEEE Trans. Power Syst.*, vol. 28, no. 4, pp. 4528–4536, Nov. 2013.
- [29] D. Kosterev et al., "Load modeling in power system studies: WECC progress update," in Proc. IEEE Power Energy Soc. Gen. Meet. Convers. Del. Elect. Energy 21st Century, Pittsburgh, PA, Jul. 20–24, 2008.
- [30] "Reliability Developing guideline: load data," North Reliabil-Electric position American Corporation, Tech. Rep., Mar. 2017 [Online]. Available: https://www.nerc.com/comm/RSTC_Reliability_Guidelines/ Reliability_Guideline_-_Load_Model_Composition_-_2017-02-28.pdf
- [31] "Electromagnetic Transient Modeling for BPS Connected Inverter-Based Resources— Recommended Model Requirements and Verification Practices: NERC Reliability Guidelines," North American Electric Reliability Corporation, Tech. Rep., Mar. 2023.
- [32] D. Kosterev, "Next steps load modeling," 2017, Accessed: Oct. 23, 2023. [Online]. Availhttps://www.nerc.com/comm/PC/LoadModelingTaskForceDL/ able: NERC_LMTF_-_Next_Steps_in_Load_Modeling_-_Kosterev.pdf
- [33] P. Mitra, L. Sundaresh, and D. Ramasubramanian, "Stability of inverter-based resource (IBR) dominated systems with different types of local loads," *CIGRE Sci & Eng.*, no. 28, Mar. 2023.
- [34] Q. Huang and V. Vittal, "Application of electromagnetic transient transient stability hybrid simulation to FIDVR study," *IEEE Trans. Power Syst.*, vol. 31, no. 4, pp. 2634–2646, Jul. 2016.

- [35] K. G. Ravikumar, S. Manson, J. Undrill, and J. H. Eto, "Analysis of fault-induced delayed voltage recovery using EMTP simulations," in *Proc. IEEE/PES Transmiss. Distribution Conf. Expo.*, Dallas, TX, May. 3–5, 2016.
- [36] S. S. Venkata and A. Pahwa, Electric Power and Energy Distribution Systems: Models, Methods, and Applications. John Wiley & Sons, 2022
- [37] H. N. Villegas Pico and V. Gevorgian, "Blackstart capability and survivability of wind turbines with fully rated converters," *IEEE Trans. Energy Convers.*, vol. 37, no. 4, pp. 2482–2497, Dec. 2022.
- [38] S. Roy and H. N. Villegas Pico, "Transient stability and active protection of power systems with grid-forming PV power plants," *IEEE Trans. Power Syst.*, vol. 38, no. 1, pp. 897–911, Jan. 2023.
- [39] North American Electric Reliability Corporation, "Statement of the North American Electric Reliability Corporation," in 2021 Ann. Rel. Tech. Conf., Sep. 2021. [Online]. Available: https://www.ferc.gov/media/nerc-panel1
- [40] "Performance, Modeling, and Simulations of BPS-Connected Battery Energy Storage Systems and Hybrid Power Plants: Reliability Guidelines," North American Electric Reliability Corporation, Tech. Rep., Jun. 2023.
- [41] P. Denholm, J. Eichman, and R. Margolis, "Evaluating the Technical and Economic Performance of PV Plus Storage Power Plants," Nat. Renewable Energy Lab., Tech. Rep. NREL/TP-6A20-68737, Aug. 2017.
- [42] P. C. Krause, O. Wasynczuk, S. D. Sudhoff, and S. Pekarek, *Analysis of Electric Machinery and Drive Systems*, 3rd ed. New York, USA: Wiley-IEEE Press, 2013.
- [43] Federal Energy Regulatory Commission, "FERC Order No. 2023: Improvements to Generator Interconnection Procedures and Agreements," Jul. 2023. [Online]. Available: https://www.ferc.gov/media/e-1-order-2023-rm22-14-000
- [44] Frequency and Voltage Protection Settings for Generating Resources, NERC PRC-024-3, Jul. 2020.
- [45] M. Chandorkar, D. Divan, and R. Adapa, "Control of parallel connected inverters in standalone ac supply systems," *IEEE Trans. Ind. Appl.*, vol. 29, no. 1, pp. 136–143, Feb. 1993.
- [46] W. Du et al., "A comparative study of two widely used grid-forming droop controls on microgrid small-signal stability," *IEEE Trans. Emerg. Sel. Topics Power Electron.*, vol. 8, no. 2, p. 963–975, Jun. 2019.
- [47] H. Jain, G.-S. Seo, E. Lockhart, V. Gevorgian, and B. Kroposki, "Blackstart of power grids with inverter-based resources," in *Proc. IEEE Power Energy Soc. Gen. Meeting*, Montreal, QC, Canada, Aug. 2–6, 2020.
- [48] Simple Solar Farm Model, Manitoba Hydro International, Manitoba, Canada, Jun. 2019, (accessed Mar. 25, 2023). [Online]. Available: https://www.pscad.com/knowledge-base/article/521
- [49] M. G. Villalva, J. R. Gazoli, and E. R. Filho, "Comprehensive Approach to Modeling and Simulation of Photovoltaic Arrays," *IEEE Trans. Power Electron.*, vol. 24, no. 5, pp. 1198–1208, May. 2009.
- [50] HVAC School, USA, See What's Inside a Reciprocating Compressor. (Jul. 11, 2018). Accessed: May. 12, 2023. [Online Video]. Available: https://www.youtube.com/watch?v=F12WccGuiSw.
- [51] S.-R. Hsieh and S. W. Shaw, "The dynamic stability and nonlinear resonance of a flexible connecting rod: Continuous parameter model," *Nonlinear Dyn.*, vol. 4, pp. 573–603, Dec. 1993.
- [52] P. C. Krause, "Simulation of unsymmetrical 2-phase induction machines," *IEEE Trans. Power App. Syst.*, vol. 84, no. 11, pp. 1025–1037, Nov. 1965.
- [53] B. Lesieutre, D. Kosterev, and J. Undrill, "Phasor modeling approach for single phase A/C motors," in 2008 IEEE Power & Energy Soc. General Meeting, Pittsburgh, PA, Jul. 20–24, 2008.
- [54] "Load modeling task force (LMTF)," Accessed: Jan. 5, 2024. [Online]. Available: https://www.nerc.com/comm/PC/Pages/Load%20Modeling% 20Task%20Force%20(LMTF)/Load-Modeling-Task-Force.aspx
- [55] S. Akbari, F. Fallahi, and T. Pirbodaghi, "Dynamic analysis and controller design for a slider–crank mechanism with piezoelectric actuators," J. Comput. Des. Eng., vol. 3, no. 4, pp. 312–321, Jun. 2016.
- [56] S. Xiao, Q. Xiao, M. Song, and Z. Zhang, "Dynamic analysis for a reciprocating compressor system with clearance fault," *J. Appl. Sci.*, vol. 11, no. 23, p. 11295, Nov. 2021.
- [57] B. P. Rasmussen and A. G. Alleyne, "Dynamic modeling and advanced control of air conditioning and refrigeration systems," University of Illinois at Urbana-Champaign, Tech. Rep., Jun. 2006.
- [58] D. Ndiaye and M. Bernier, "Dynamic model of a hermetic reciprocating compressor in on-off cycling operation," *Appl. Thermal Eng.*, vol. 30, no. 8, pp. 792–799, 2010.

- [59] "Bristol reciprocating compressor H22J363ABCA," Accessed: May.4, 2023. [Online]. Available: https://www.insco.com/2580858/p/n/bristol-compressors-h22j363abca
- [60] "Installation and service intructions refrigerationair conditioning/heat pump compressors," Accessed: Oct. 11, 2023. [Online]. Available: https://www.bristolcompressors.com/data//installation_and_ service/uploads/IMG-1600429622597.pdf
- [61] S. Zocholl and G. Benmouyal, "On the protection of thermal processes," IEEE Trans. Power Del., vol. 20, no. 2, pp. 1240–1246, Apr. 2005.
- [62] J. R. Marti, "Accurate modeling of frequency dependent transmission lines in electromagnetic transient simulations," *IEEE Trans. Power App. Syst.*, vol. PAS-101, pp. 147–155, Jan. 1982.
- [63] "Datasheet single-phase induction motor squirrel cage rotor," Accessed: Oct. 11, 2023. [Online]. Available: https://dealerselectric.com/images/Products/WEG/00536OS1DCD56H-S.pdf
- [64] H. N. Villegas Pico, B. Mather, and G.-S. Seo, "Model identification of inverter nonlinear control dynamics," in 2018 IEEE Electron. Power Grid (eGrid), Charleston, SC, USA, Nov. 2018, pp. 1–6.
- [65] LENNOX, "Scroll compressor," [Online]. Available: https://www.lennox.com/buyers-guide/guide-to-hvac/glossary/scroll-compressor, (accessed Sep. 30, 2023).



Abdelrahman M. Mannan (Graduate Student Member, IEEE) received the B.Sc. and M.Sc. degrees in electrical engineering from Iowa State University (ISU), Ames, IA, in 2021 and 2023 respectively. At present, he is an electrical engineer at Black & Veatch in the Engineering Development Services sector.

His research interests include hybrid PV plants, power system modeling, and EMT simulation; renewable energy integration; and grid-forming technologies.



Hoang P. Dang (Graduate Student Member, IEEE) received the B.Sc. degree in electrical engineering from Iowa State University (ISU), Ames, IA, in 2021. At present, he is a PhD student in the electric power and energy systems group within the Department of Electrical and Computer Engineering at ISU.

His research interests include power system modeling, EMT simulation, and control; renewable energy integration; and power restoration processes.



Hugo N. Villegas Pico (Senior Member, IEEE) earned the degree of Ingeniero en electrónica, automatización y control from Universidad de las Fuerzas Armadas - ESPE, Sangolquí, Ecuador, in 2008, the M.S. degree in electrical engineering from Iowa State University, Ames, IA, USA, in 2011, and the Ph.D. degree in electrical and computer engineering from Purdue University, West Lafayette, IN, USA, in 2016.

At present, Hugo is a Harpole-Pentair Assistant Professor in the Department of Electrical and Com-

puter Engineering at Iowa State University. Hugo's research interests lie at the intersection of renewable energy conversion, power system dynamics and protections, power restoration processes, and control systems. Hugo was the recipient of the Fulbright scholarship from 2009 to 2011, the Best paper award by the IEEE Transactions on Energy Conversion for 2013–2014, the IEEE Power & Energy Society Prize paper award for 2015, and the National Science Foundation CAREER award in 2024.